A Study of Astronomical Polarization, Polarimetric Observations and Polarimetry of Exoplanets

Master's Thesis
University of Turku
Dept. of Physics and Astronomy
Astronomy
2020
BEng Yasir Abdul Qadir
Reviewed by:
Dr. Andrei Berdyugin
Prof. Juri Poutanen

The originality of this thesis has been checked in accordance with the University of Turku quality assurance system using Turnitin OriginalityCheck service.

UNIVERSITY OF TURKU
Department of Physics and Astronomy
ABDUL QADIR, YASIR A Study of Astronomical Polarization, Polarimetric Observations and Polarimetry of Exoplanets
Master's Thesis, 51 pages
Astronomy
March 2020
The originality of this thesis has been checked in accordance with the University of Turku quality assurance system using the Turnitin OriginalityCheck service

---

Astronomical polarization has become one useful tool to study a number of astronomical objects and related astrophysical mechanisms. The polarization of electromagnetic waves is caused by various astronomical phenomena. One such phenomenon is when the light emitting from a planet(s) hosting star is reflected by the orbiting planet(s). However, the degree of polarization due to such events is tiny and their observations require highly sensitive polarimeters. DiPol-2 is a one such high sensitivity polarimeter that can measure polarization degree of more than 10^{-5}. The polarimeter is presently installed with T60 telescope at Haleakalā observatory in Hawaii and is operated remotely by Physics and Astronomy department at University of Turku.

We used DiPol-2 to observe a hot Jupiter exoplanet named υ And b in B, V and R passbands. These observations were made using the combination of T60 and DiPol-2. It was the first time that these instruments were used together to record polarimetric observations of an exoplanet. Stokes parameters describe the state of polarization and variations in these parameters can help to deduce orbital parameters and/or stellar, planetary characteristics. This process however requires that data visualization to be compared with numerous models that have been developed to interpret polarimetric observations. The polarimetric observations started in the second half of 2016 and continued till early 2019. We observed the target whenever observing time allocation and observation conditions allowed it. The observational data then went through a lengthy process of data transfer and data reduction.

For data analysis, Lomb-Scargle algorithm was used to deduce orbital periods present in the data. Lomb-Scargle periodogram showed a number of peaks with different orbital periods. It was deduced that the presence of multiple orbital periods was due to magnetic activity on the stellar surface that contaminated polarimetric signals of the exoplanet. To further visualize the data, curve fitting was performed using Fourier series in order to deduce orbital peaks and estimate planetary albedo. We were able to estimate values for a few parameters but at this point it has not been possible to separate planetary signal from the stellar signal. This task would require a sophisticated model and that was beyond the scope of this study.

Keywords: Polarization, astronomical polarimetry, Stokes parameters, DiPol-2, exoplanets, polarimetric observations, starspots, stellar polarization, υ And, planetary albedo, Lomb-Scargle periodogram, Fourier Series, Curve Fitting.

Contents

1 Introduction

Light can be described as a combination of transverse electromagnetic waves that consist of an electric and a magnetic component. The most common sources of light such as Sun, electric lamps, fire flames, etc., emit unpolarized light. An electromagnetic wave emitted by these sources is generated by electric charges that vibrate randomly in all possible directions. Therefore, the resultant electromagnetic waves also vibrate in all possible directions and referred as unpolarized light waves.

A polarized wave has certain types and one of these types is *linearly* polarized light wave. In this type of polarized wave, the vibrations are confined in a single plane. The transformation of an unpolarized light wave into fully or partially polarized light wave is known as *polarization*. The process of measurement and interpretation of the polarization of electromagnetic radiation is called *polarimetry* and the instrument used for this purpose is known as *polarimeter*. The first systematic observations of polarization of starlight have been started by William Hiltner and John Hall in 1949. But it took a couple of decades for optical polarimetry to become one of the mainstream methods in observational astrophysics. This was made possible due to the introduction of highly sensitive detectors in optical photometry and spectroscopy.

Astropolarimetry has now become an important method of studying of large variety of astrophysical objects. A number of physical mechanisms can produce different types of polarization by various degrees. Thus, by detecting and measuring the polarization of astronomical light, we can draw important conclusions on the nature of physical phenomena, ranging from structure of galactic magnetic fields to the atmospheric composition of exoplanets.

1.1 Polarization: Basics

The electric and magnetic components of any given electromagnetic wave are always perpendicular to each other they are also perpendicular to the direction of wave propagation (see Figure 1). At optical wavelengths, the direction of polarization

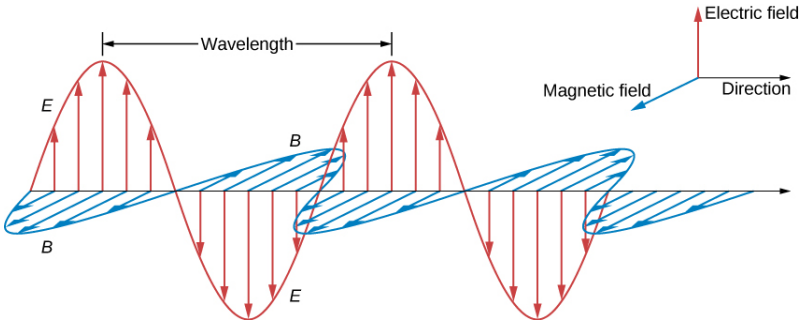

Figure 1. An illustration of electromagnetic wave emitted by single charged particle oscillating in fixed direction. Electric field, magnetic field and direction of propagation are shown in red, blue and black colors respectively.

refers to the direction in which electric field oscillates. In Euclidean coordinates (x, y, z), the electric field $\mathbf{E}$ traveling in direction z can be described as:

$$\mathbf{E}(t, z) = \mathbf{E}(0, 0)\cos(\omega t - kz - \phi), \tag{1}$$

where t is time, ω is the angular frequency, $k = \omega/c$ is absolute value of the wave vector and ϕ represents an arbitrary phase. For the simplicity purposes, location of $\mathbf{E}(t)$ is considered in only xy plane, i.e. $z = 0$. Then, the decomposition of $\mathbf{E}(t, z)$ into x and y components can be written as following:

$$\begin{aligned} E_x(t) &= E_x(0)\cos(\omega t - \phi_1), \\ E_y(t) &= E_y(0)\cos(\omega t - \phi_2), \end{aligned} \tag{2}$$

where ϕ_1 and ϕ_2 denote two a priori arbitrary phases. The angle between $\mathbf{E}(t)$ and positive x-axis is denoted by χ (Figure 2, left) and counted in counterclockwise direction is known as *polarization angle*. The polarization of an electromagnetic wave is given by the relative values of $E_x(0)$, $E_y(0)$ (Figure 2, right), ϕ_1 and ϕ_2.

1.1.1 Types of Polarization

Elliptical polarization is the most common type of polarization of an electromagnetic wave in which the projected path of electric field vector looks like an ellipse (Figure 3, right). In an elliptically polarized electromagnetic wave, the electric field has two perpendicular linear components that can have any amplitude and/or any phase difference. The ellipse keeps constant orientation in time with respect to xy plane. For elliptical polarization, the polarization angle χ is defined as the angle

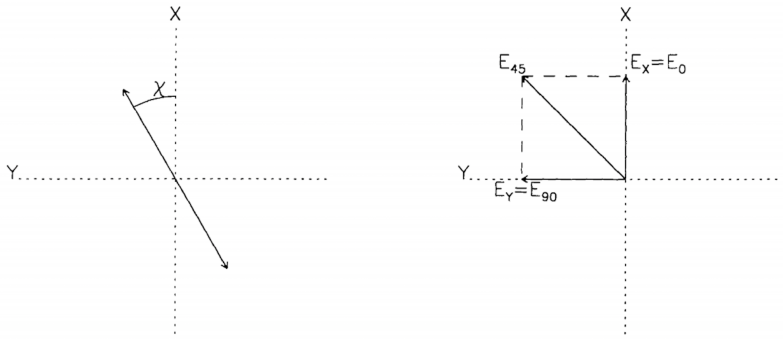

Figure 2. An illustration of position angle χ and electric field components. Left: linear polarization at position angle χ measured counter clockwise from x-axis. Right: electric field components at 0°, 45° and 90°.

between semi-major axis of the ellipse and positive x-axis. The direction in which electric field rotates describes the polarization as either right or left hand elliptical polarization.

Linear polarization happens if the ellipse of polarization is degenerated into a line. In Figure 3 (left), the oscillation of electric field is confined in a single plane that does not change as the electromagnetic wave propagates. An electromagnetic wave that is linearly polarized has no phase difference, i.e., $\phi_1 = \phi_2$. For $\phi_1 = \phi_2 = 0$:

$$\begin{aligned} E_x(t) &= E_x(0)\cos(\omega t), \\ E_y(t) &= E_y(0)\cos(\omega t). \end{aligned} \tag{3}$$

The orientation of electric field **E** depends only on the magnitudes of $E_x(0)$ and $E_y(0)$ and has no direction. The plane of polarization is given by the angle χ, which remains constant between 0 and π.

Circular polarization is one special case in which ellipse of polarization degenerates into a circle (Figure 3, middle). In this type of polarization, the electric field has two perpendicular linear components, which are equal in amplitude and have a phase difference of $\pi/2$. In other words $\phi_2 = \phi_1 \pm \pi/2$ and for $\phi_1 = 0$, $E_x(0) = E_y(0)$:

$$\begin{aligned} E_x(t) &= E_x(0)\cos(\omega t), \\ E_y(t) &= \pm E_y(0)\sin(\omega t), \end{aligned} \tag{4}$$

where positive and negative signs of $E_y(t)$ represent counterclockwise and clockwise

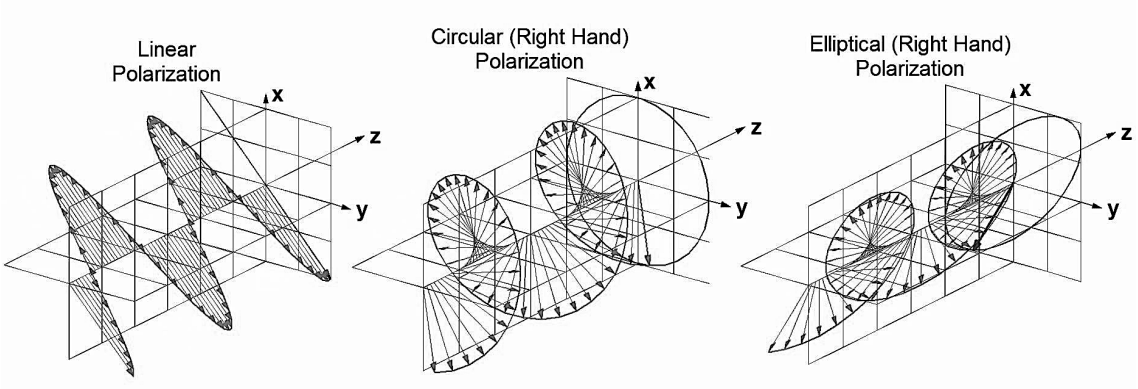

Figure 3. Left: Linear polarization is when the oscillation of electric field is confined in a plane. Middle: Circular polarization in which electric field components with a phase difference of 90° appear to rotate counter clockwise to an observer for right hand polarization. Right: Elliptical polarization in which electric field components with any amplitude and/or any phase difference appear to rotate counter clockwise to an observer for right hand polarization.

motions respectively. The movement of electric field vector in the xy plane is in a circular motion with angular frequency ω. The direction of electric field rotation describes the polarization as either right or left hand circular polarization.

1.1.2 Stokes Parameters

In the previous section, it is mentioned that the polarization state of an electromagnetic wave depends on amplitude of electric field components $(E_x(0), E_y(0))$ and phase difference $(\delta = \phi_2 - \phi_1)$. By using Stokes parameters, these quantities are quantified into characteristic intensities. This is done due to the fact that astronomical observations measure light intensities and not field amplitudes. The *normalized Stokes parameters* q, u and v are defined as follows:

$$\begin{aligned} q &= Q/I, \\ u &= U/I, \\ v &= V/I, \end{aligned} \tag{5}$$

where Q, U, V are *absolute Stokes parameters* and I is intensity of the wave. In terms of electric field components, these parameters are described as:

$$\begin{aligned} I &= E_x^2 + E_y^2 = E_{0^\circ}^2 + E_{90^\circ}^2, \\ Q &= E_x^2 - E_y^2 = E_{0^\circ}^2 - E_{90^\circ}^2, \\ U &= 2(E_x E_y \cos\delta) = E_{45^\circ}^2 - E_{-45^\circ}^2, \\ V &= 2(E_x E_y \sin\delta) = E_{LCP}^2 - E_{RCP}^2. \end{aligned} \tag{6}$$

Stokes I simply represents the total power of incoming radiation. This is done by sampling two orthogonal polarizations at any two orthogonal angles of either elliptical or linear or circular polarization and their summed powers give the total intensity. *Stokes Q* is the difference of intensities in x and y that partly describes linear polarization. Suppose, incoming electric field is vertically polarized then using Equation (6): $Q = I$ and when the polarization is horizontal: $Q = -I$. But for $\chi = 45^\circ$: $Q = 0$, this parameter does not show any polarization. *Stokes U* quantifies the difference between two orthogonal angles of 45° and $135^\circ(-45^\circ)$. Therefore, to completely describe linear polarization both *Stokes Q* and *Stokes U* are needed. The relationship between Stokes parameters and linear polarization is as follows:

$$\begin{aligned} P_L &= \sqrt{Q^2 + U^2}/I, \\ \chi &= \frac{1}{2}\,\mathrm{atan}\left(\frac{U}{Q}\right), \end{aligned} \tag{7}$$

where P_L is degree of linear polarization and χ is polarization angle, which give length and the orientation of a vector that is centered at the origin of plane spanned by *Stokes Q* and U, while atan is quadrant-preserving arctangent.

Finally, *Stokes V* corresponds to the circularly polarized intensity. As briefly mentioned earlier, there are two types of circular polarizations opposite to each other, named as *left hand circular polarization* (LCP) and *right hand circular polarization* (RCP). To the observer, LCP appears to be rotating clockwise and RCP appears as rotating counterclockwise. The difference between squared values of these two is V. The relationship between degree of circular polarization P_C and *Stokes V* is given as:

$$P_C = V/I. \tag{8}$$

For individual waves, Stokes parameters are related as:

$$I^2 = Q^2 + U^2 + V^2. \tag{9}$$

In some texts, *Stokes* I, Q, U, V are also referred as S_0, S_1, S_2, S_3 or S_1, S_2, S_3, S_4. The degree of polarization in optical astronomy is written in units of per cent (%) or in decimal fractions of the total intensity.

1.2 Polarization: Instrumentation

Just like any other optical astronomy observations, first and foremost instrument needed to conduct polarimetric observations is a telescope. However, the design and geometry of any given telescope is going to have an influence on the state of polarization for the collected light. There may be some exceptions in the case of highly symmetric situations. It is crucial to take into account the conditions and configurations that can modify polarization state and make such arrangements that these modifications can be minimized. Other than a telescope, polarimetric observations require the use of a *polarimeter*.

Polarimeter is an instrument that can either measure or determine the normalized Stokes parameters. It generally consists of two main parts: a *polarization modulator* and *polarization analyzer*. A modulator performs modulation of the polarization state of an incident light beam by any given frequency and an analyzer separates two orthogonally polarized components of electromagnetic wave. The third component of the polarimeter that is also common to other instruments, such as photometer or spectrograph, is a *detector*. The detector measures the intensities of these polarized components synchronously with the modulation frequency.

1.2.1 Modulators: Constant and Variable Phase-Shift Retarders

In the optical spectral region, modulation is quite essential for the accurate polarimetric observations. Most modulators employ a technique that is based on the *phase retardation or phase shift* between the two orthogonal components of polarization for the incoming light beam. This modulator, called *retarder* can either introduce a *constant* or *variable* phase shift.

The constant phase shift retarders, also known as *wave plates* are made of a uni-axial birefringent crystal, which is cut so that the optical axis (minimum refraction index direction) is parallel to the plate surface. There are two types of wave plates widely used in astropolarimetry: quarter wave plates (QWP) with the phase shift $\pi/2$ and

half wave plates (HWP) with the phase shift π. QWP is used to change circularly polarized light wave into linearly polarized light wave and HWP is used to rotate the polarization plane of a linearly polarized light wave.

Two types of variable phase shift retarders are used in astropolarimetry: photo-elastic (piezoelectric) modulators (PEMs) and ferro-electric liquid crystals (FLCs). PEM is made with a material that is non-birefringent slab stressed at the natural slab frequency of f_0 with the piezoelectric transducer. At the base frequency of f_0, PEM acts like a variable QWP that has time variable phase shift from 0 to $\pi/2$ and thus allows the circular polarization to measured directly. In a case, when PEM is driven to the frequency of $2f_0$, it acts like HWP and thus allows direct measurement of linear polarization. A thin layer of a material made of liquid crystal is used to manufacture FLC modulator and this layer is placed between the two glass plates. For astropolarimetry, FLCs are used that are capable to switch orientation of the optical axis but they have a fixed retardation π. The optical axis can be controlled with applied drive voltage in order to measure linear polarization just as PEMs. FLC can be operated at the frequencies up to few KHz and is more efficient in comparison with PEM due to capability to provide a nearly square-wave modulation.

1.2.2 Analyzers: Single and Double-Beam Units

The simplest form of a *single-beam* analyzer is well-known polaroid made by hematite crystals and either aligned in the direction of a thin film of polymeric transparent or layered on a surface of glass. *Optical dichroism* is a property of polaroid that means strong absorption for linearly polarized light in the direction that is parallel to the orientation of crystal axis. When a polaroid is rotated, it acts as a single-beam analyzer for the light that is linearly polarized. The more advanced single-beam analyzers are *Nicol* and *Glan-Thompson* prisms made of calcite. In these prisms, one of the orthogonally polarized beam is either completely absorbed or deflected.

Major disadvantage of the single-beam analyzer is the loss of half of the intensity from incoming light beam. To overcome this issue, the *double-beam analyzers* or *polarization beam-splitters* are frequently employed in optical astropolarimetry. They are made of birefringent crystals such as calcite, quartz or magnesium fluoride. Double-beam analyzer splits the incident light beam into two orthogonal polarized beams so that both of them can be measured simultaneously. The most frequently used double-beam analyzers are *plane-parallel calcite plate*, *Savart plate* and *Wollaston prism*. Plane-parallel and Savart plate split the incident light beam into two different beams in parallel direction and Wollaston prism diverts the two beams symmetrically.

1.2.3 Detectors

Optical polarimetry uses mostly three types of detectors: CCD cameras, photomultipliers (PMTs) and avalanche photodiodes (APDs). These detectors have their own advantages and disadvantages.

In optical polarimetry, the most common detectors are *charge-coupled device* CCD cameras. The main advantages of CCD camera are their high quantum efficiency (QE), wide variety and convenient data acquisition. Furthermore, they consists of panoramic (multi-cell) registration devices. This allows the recording of either two orthogonal polarized stellar images or spectra on a single detector simultaneously. For low-budget polarimetric instrumentation, the small-sized CCD cameras with thermoelectronic cooling are used. These cameras are portable and connected to control computer by universal serial bus (USB) port. For broadband polarimetry using CCDs, the data reduction is performed by applying standard *aperture photometry* method. This means that CCD images are calibrated by subtraction of dark, bias and flat-fielding, then the sky contribution is subtracted and the intensity of orthogonally polarized stellar images are measured. CCD cameras do have their shortcomings such as early pixel saturation for bright celestial objects due to relatively small full-well capacity and long time required for the image readout.

PMTs can register high fluxes, instant readout and have dynamical range. Polarimetry requires high amount of photons and pixel saturation issue for bright objects in CCD polarimeters can sometimes make the PMT a preferred choice. PMTs can be also easily used in combination with the high-frequency modulators such as FLCs and PEMs. The disadvantages of PMT detectors are relatively low. In comparison with CCD camera, the quantum efficiency and a single-cell detector type limits their use to polarimetry of only point-like objects, i.e., single targets. The use of diaphragm in the focal plane of telescope where the object is placed results in the polarization and intensity of sky background to be measured separately. Even though PMT detectors may be more useful in certain situations but they can not compete with CCD detectors in case of low-flux domain.

Avalanche photo-diode (APD) can be referred as semiconductor analog to the PMT. In APDs incoming photons generate electron-hole pairs and large reverse bias voltage accelerates photoelectrons. When these electrons have a collision with the atomic lattice, secondary electrons are released by secondary ionization and an avalanche of charge carriers occurs when these electrons accelerate. APDs can tolerate even higher fluxes than PMTs. As compared to PMTs, they have higher QE in near IR but lower in blue wavelengths. APD detectors are better suited for polarimetry

of the brightest objects that require high precision in near infra-red wavelengths. But their efficiency in blue and visual spectra when compared to PMTs is about similar. The dark current is higher in APDs, which often makes them noisier than other detectors. Their small effective photosensitive area requires a extreme precision when positioning the telescope exit pupil on the surface of detector. Due to these shortcomings, APDs are the least popular type of detectors in optical polarimetry.

1.3 Polarization: Astrophysical Mechanisms

A number of astrophysical mechanisms such as emission, reflection, absorption, scattering or influence of magnetic fields may affect or alter the polarization state of a photon. Thus, polarimetry can help deduce information on physical properties of any astronomical object that emits the light. Moreover, the polarimetry can also provide information on properties of the circumstellar and interstellar medium with which the passing light interacts.

There are two fundamental types of emission known in astrophysics: *thermal* and *non-thermal* ones. The radiation emitted by thermal emissions is purely due to the temperature of source. Any object that has a temperature above absolute zero emits thermal radiations. In this phenomenon, atoms move with respect to each other in different directions and at varying speeds. As a result, their collisions produce isotropically emitted radiation when electrons change energy states within an atom. The continuous spectrum of thermal emission is described by Planck's law. According to Planck's law, a spontaneous and continuous emission of electromagnetic radiation occurs in every physical body and the spectral radiance of a given body B is the amount of energy that it emits at various frequencies of the radiation (Planck 1901):

$$B(\nu, T) = \frac{2h\nu^3}{c^2} \frac{1}{e^{h\nu/k_B T} - 1}, \tag{10}$$

where ν is frequency, T is absolute temperature, k_B is Boltzmann constant, h is Planck constant and c is speed of light. For heated gases or solid bodies, the thermal emission is incoherent, isotropic, and unpolarized. The non-thermal emission includes any emitted radiation that does not depend on temperature of the source. Synchrotron radiation is an example of non-thermal emissions that is generated by free electrons that spiral at relativistic speeds around magnetic field lines. Synchrotron radiation is naturally linearly polarized in the plane of the electron orbit.

Light-to-matter interaction is perhaps the most important mechanism that produces astrophysical related polarization. By studying the polarization of light reflected by

a surface or atmosphere of celestial body can help to deduce the size, shape, chemical composition, atmospheric structure and stratification of that body. Scattering of light by particles such as electrons, atoms, molecules and dust grains is quite a common phenomenon that can alter the polarization state of an electromagnetic wave. All types of scattering such as Thomson, Compton, Inverse Compton, Rayleigh, Raman etc., cause linear polarization.

Figure 4 illustrates the geometry of scattering polarization, which is true for any scattering regime regardless of their distinct physical mechanisms. Let us assume incident unpolarized light with electric field components E_x, E_y in x and y directions respectively and propagating in z direction. After the interaction, the direction of propagation changes in the yz plane with an angle θ to the z-axis. For observer of this scattered light, the light intensities remian same in x direction before and after the scattering, i.e., $E_x'^2 = E_x^2$, where prime represents the scattered light. The y component, however, transforms as $E_y'^2 = E_y^2 \cos^2\theta$, which means the reduction in by a factor of $\cos^2\theta$, i.e. the scattering has caused linear polarization and the degree of polarization (P_L) is:

$$P_L = \frac{I'_x - I'_y}{I'_x + I'_y} = \frac{1 - \cos^2\theta}{1 + \cos^2\theta}, \tag{11}$$

where, I'_x and I'_y are observed intensities. (Trippe 2014)

The understanding of astrophysical objects such as stars or galaxies is incomplete without the consideration of magnetic fields. Sufficiently strong magnetic field results into *Zeeman effect* in which a spectral line may split into several polarized components with different splitting and strength as a consequence of magnetic field being present. The intensity profile is usually split into two or more components and this separation is linearly increases with the magnetic strength. In this situation, the component of magnetic field along the line of sight (longitudinal field B_z) produces a non-zero circular polarization signal. In the weak field regime, *Stokes* v is given by Bagnulo and Landstreet (2015):

$$v = -g_{\rm eff} C_z \lambda^2 \frac{1}{I} \frac{dI}{d\lambda} B_z, \tag{12}$$

where $g_{\rm eff}$ is the effective Landé factor, I is intensity at wavelength λ and $C_z = 4.67 \times 10^{-13} \text{Å}^{-1} G^{-1}$.

The transverse component of magnetic field is related to linear polarization in such a

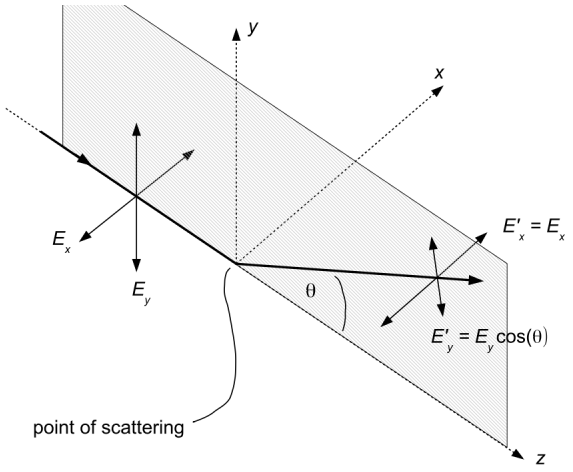

Figure 4. A light ray that is unpolarized has linear polarization components E_x, E_y propagating in z direction. It gets scattered by an angle θ and becomes linearly polarized. The propagation direction changes to yz plane (shaded). For observer, the polarization components of the scattered light are perpendicular to the direction of propagation, i.e., $E'_x = E_x$ and $E'_y = E_y \cos\theta$. Image from S. Trippe (2014).

way that with the strength of magnetic field linear polarization increases quadratically. It is given (Bagnulo and Landstreet 2015):

$$\begin{aligned} q &= -\frac{1}{4} g_{\rm eff}^2 C_z^2 \lambda^4 \frac{1}{I} \frac{d^2 I}{d\lambda^2} B_\perp^2 \cos 2\chi, \\ u &= -\frac{1}{4} g_{\rm eff}^2 C_z^2 \lambda^4 \frac{1}{I} \frac{d^2 I}{d\lambda^2} B_\perp^2 \sin 2\chi, \end{aligned} \tag{13}$$

where χ is azimuthal angle of the magnetic field and $B_\perp$ is transverse component of the magnetic field.

When the magnetic field is not weak, Faraday rotation is responsible for a non-negligible rotation of the polarization plane. In this case, it is not possible to describe certain properties of the Stokes profiles with simple analytical considerations. For example, circular and linear polarizations do not increase linearly and quadratically with the field strength. However, Stokes profiles may still be calculated numerically (Wade et al 2001) or using the hypothesis of Milne–Eddington approximation.

1.4 Polarization: Astrophysical Sources

All types of stars given by Hertzsprung-Russell (HR) diagram are known to possess magnetic fields and they can be studied with spectropolarimetry. Active stars have been observed to posses multiple stellar spots, which can be studied by spectroscopic and photometric observations (Yakobchuk and Berdyugina 2018). These starspots also contribute to polarization. The binary stars are another topic of interest to be studied by optical polarimetry. Their gravitational interaction may involve matter transfer from one component to the other. This often results in linear polarization that varies due to the light scattering on the circumstellar material (Zellner and Serkowski 1972). In case of black hole being one of the component in a binary system, synchrotron radiation may result in linear polarization emitted in the jet. This means that polarimetry can reveal useful details of the phenomenon and physical properties of material forming gaseous streams, discs, jets and non-spherical envelopes.

Planetary bodies reflect the light emitted by their host stars. The scattering of light either by a solid surface or by an atmosphere makes it partially linearly polarized. *Umov effect* is a due to the interplay of absorption and scattering of light, which is anti-correlation between linear polarization ($\bar{p_L}$) and geometric albedo p (measurement of light that gets reflected by the surface of a celestial object) of a solid surface is given as (Bowell & Zellner 1974):

$$\log(p) = -c_1 \log(\bar{p_L}) + c_2, \tag{14}$$

where c_1 and c_2 are two constant parameters and their values depend on the structure of surface material. For very low albedos, $c_1 \approx 1$, $c_2 \approx -2$, Equation (14) gives the degree of polarization close to 100% and thus any observed deviation from this relationship represent structural change of the surface material (Trippe 2014). Oceans, even though having a low albedo, may produces highly polarized *glint* light due to their specular reflection. Theoretically, it is even possible to detect extra terrestrial life using (spectro)polarimetry by looking for circularly polarized light reflected from certain biological substances.

Interstellar and circumstellar space is filled with diffuse matter which is presented in a various states ranging from cold molecules and dust grains to hot ionized atoms and free electrons. The interaction of light with this matter may cause polarization of scattered light by varying degree. The well-known result of such interaction is an *interstellar polarization* of distant stars which is produced by dust grains that are non-spherical and they are aligned by interstellar galactic magnetic field. Because the

direction of interstellar polarization coincides with the direction of galactic magnetic field lines, polarimetry is used for studying the structure of the interstellar magnetic fields on the large and small scales.

The other prominent astrophysical sources that show polarization are space masers, pulsars, active galactic nuclei (AGN), gamma ray bursts (GRB) and cosmic microwave background (CMB). Space masers emit *stimulated* linearly polarized radiation at radio frequencies. Pulsars emit both thermal and non-thermal radiations, but predominantly the later one. Synchrotron-dominated radiation shows both linear and circular polarization. AGNs are the most luminous objects in the universe and they emit in multiple wavelengths. They show a linear polarization mostly due to synchrotron sources together with a small presence of circular polarization. In GRBs, substantial linear polarization is produced due to synchrotron mechanism. CMB shows two types of polarization. The *electric-field like* polarization is perpendicular to the gradient of a local perturbation, shows no handedness and is caused by local energy density fluctuations. The *magnetic-field like* polarization shows a local curl pattern with distinct handedness. They are caused by tensor perturbations as a result of gravitational waves propagating through CMB plasma.

2 Exoplanets

Extra solar planets (or *exoplanets*) are planets that exist beyond our solar system. In the last couple of decades, exoplanets have been discovered in all sizes ranging from bigger than Jupiter to smaller than the Earth. Some of these exoplanets orbit so close to their host starts that their surface temperatures can melt iron but others are as far as 2000 astronomical units (AU) from their parents stars. There are just a few cases in which the exoplanets have been imaged directly. An overwhelming majority of exoplanets discovered to date have been discovered by *indirect* detection methods such as *Doppler spectroscopy* (radial velocity or RV) method, transit method, astrometric measurements and gravitational micro-lensing.

In general, the amount of light reflected by an exoplanet is a very small fraction of the radiation coming out of the host star. This makes exoplanets very difficult for direct detection as they are completely out shined by their parent stars. The starlight is in most cases is unpolarized but it becomes partially polarized when reflected by a planet. Thus, polarimetry can be used to detect and reveal certain physical characteristics of exoplanets. However, even if the light that is reflected by an exoplanet becomes 100% polarized, it is still going to be a tiny fraction of resulting polarization in the total light coming out of that solar system. Therefore, the polarimetric detection is presently only possible for planets that are big in size and orbit close to their host stars.

Since polarimetry is comparatively a newer tool to investigate exoplanets, theoretical models that interpret polarimetric observations are still developing. These models are computed by using a number of assumptions in order to provide certain characteristics of an exoplanet, such as orbital parameters and chemical composition of the atmosphere. Theoretical models are quite essential to deduce useful information from values of measured Stokes parameters of the polarization. This chapter will discuss several such models that help interpret polarimetric observations of exoplanets.

2.1 Hot Jupiters (CEGPs)

Hot Jupiters or close-in extrasolar giant planets (CEGPs) are the gaseous giants similar to Jupiter, but unlike it, they orbit their host stars at very close distance. The typical radius of CEGP's orbit is ≤ 0.1 AU and typical orbital period is ≤ 10 days. CEGPs have dominated earlier discoveries of exoplanets as they are the easiest to be detected by Doppler spectroscopy and transit methods. They make up to $\sim$340 of more than 4000 exoplanets discovered till to date (Starr 2019).

According to present models of planetary formation, CEGPs cannot be formed at such short distance from the host star. These models predict that due to gravity, radiation, and intense stellar winds gas should not clump together to form gaseous giant in the nearest vicinity of the star. One possible explanation is that these planets are formed further away, and then migrated towards the host stars. Although formation of CEGPs may still be a mystery, their proximity to harboring stars make them very interesting objects for studying star and planet interactions.

The amount of starlight reflected by an exoplanet gets reduced by $1/d^2$, where d is the distance between the planet and host star. Thus, it becomes really difficult to detect the light scattered by an exoplanet that has an orbit far from its parent star. Furthermore, the observations of polarization from distant exoplanets would require an enormous amount of time to get repeated measurements due to the long orbital period. This is why CEGPs with small orbits and short orbital periods have become the primary choice for polarimetric observations. Their location in a planetary system, their sizes and atmospheric compositions may lead to reflection of significant portion of starlight and thus, allow detection of polarization.

Many CEGPs are so close to the host stars that stellar magnetic field is able to drive atmospheric escape through reconnection of magnetic field lines. Due to the closeness, magnetic field of CEGPs can also affect activity on the host star if it perturbs stellar open field lines. The upper atmospheres of CEGPs are expected to produce strong Rayleigh scattering and their closeness to parent stars enables them to receive a large amount of starlight flux. The short orbital period of such planets also help to gather repeated observations within a reasonable time period. All these facts make CEGPs the prime targets for polarization studies, which can help us better understand the various phenomena related to exoplanets.

2.2 Polarimetry of Exoplanets

In 2008, the earlier discovered by RV method exoplanet HD 189733b was successfully detected by polarimetry (Berdyugina et al 2008). However, no new exoplanet has ever been discovered with this technique till now. Polarization is prone to detect CEGPs with higher albedos, as in such situations the amount of reflected starlight is higher. Seager et al (2000) modeled that the degree of polarization for CEGPs is expected to be at the tens of parts-per-million level in the combined light of solar system that hosts planet(s). This implies the necessity of a polarimeter with very high sensitivity to observe such tiny levels of polarization.

The degree of polarization varies as a planet orbits the parent star due to a number of factors that are explained in the following sections. This variability can help reveal the orbital time period, orientation in space, eccentricity, inclination and composition of atmospheric particles if ant present on any given planet. (Berdyugina et al 2008; Fluri & Berdyugina 2010; Berdyugina et al 2011)

2.2.1 Orbital Period

Let us consider a basic example of a star system where the value of semi major axis of planetary orbit is higher than the radius of host star. As a result, all the starlight received by the planet is parallel and star acts like a point-source. Two different reference frames are usually employed when describing *Stokes Q* and *U* parameters. The first one is with regard to the celestial north for the observer present on Earth is called *observer's frame* in which positive *Stokes Q* denotes the light that is linearly polarized parallel to the local meridian of an observer. In the second frame of reference, the contributions from various elements of stellar surface are accounted for. Stokes parameters are defined with regard to the *scattering plane* in which the positive *Stokes Q* represents linearly polarized light perpendicular to the plane of scattering. For *Stokes* $U^{'} = 0$, *Stokes* $Q^{'}$ in the scattering plane (Fluri and Berdyugina 2010):

$$Q^{'} = \frac{pr^2}{d^2 D^2} \phi(\alpha) \sin^2 \psi, \tag{15}$$

where *prime*($'$) indicates scattering plane as reference frame, p is geometric albedo, r is planetary radius, d is the distance between an observer and star, D is the distance between planet and host star, $\phi(\alpha)$ is the phase function, ψ is scattering angle that relates to the phase angle: $\alpha = \pi - \psi$. Another angle that is present between a stellar surface element towards the orbiting planet and Earth is referred as phase

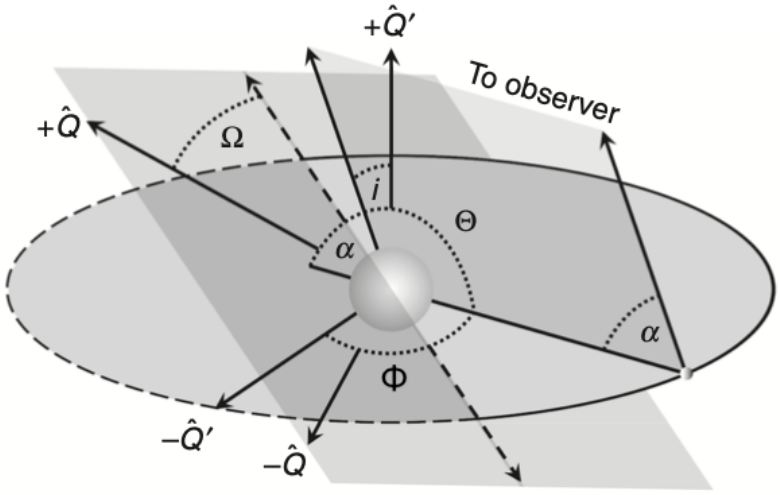

Figure 5. Orbit of a planet: where phase angle α, polarization angle θ, orbital inclination i, orbital phase ϕ and longitude of the ascending node Ω are shown. The direction of $+\hat{Q}'$ is perpendicular to the orbital plane and $-\hat{Q}'$ direction lies in the orbital plane. $+\hat{Q}$ and $-\hat{Q}$ lie in plane of the sky. Image from Wiktorowicz and Stam (2015).

angle (see Figure 5). Assuming the planet as a Lambert sphere where every incoming photons is scattered singly and isotropically, the analytical form of phase function ϕ (Russell 1916):

$$\phi(\alpha) = \frac{\sin\alpha + (\pi - \alpha)\cos\alpha}{\pi}. \tag{16}$$

Figure 5 shows that the direction $+\hat{Q}'$ is perpendicular to the orbital plane but points toward the observer only when the inclination (an angle between the orbital plane and plane perpendicular to the observer's line of sight) $i = 0°$, i.e., where the orbit is seen face-on (non transiting). For inclination $i = 90°$, the planet will transit the host star, i.e., the orbit is seen edge-on at orbital phase $\phi = 0$ for the observer. If any given CEGP system is at $i < 90°$, then the full range of phases is not visible and thus phase angle α can not be fully probed. It is estimated that only about 10% of CEGPs should have the orbital inclinations near 90° (Seager et al 2000). The $-\hat{Q}'$ direction lies in the orbital plane, $+\hat{Q}$ and $-\hat{Q}$ lie in the plane of sky and indicate celestial north and east respectively. The orbital phase is: $\phi = 2\pi(t - t_0)/T$. For circular orbits $(t - t_0)$ is the time since inferior conjunction of the planet (or mid-transit for transiting exoplanets) and T is the orbital time period.

The degree and direction of polarization depends on ψ as indicated in Equation (15). It changes along the orbital phase angle α as planet orbits the host star. Variations

in the degree of polarization from light scattered by an exoplanet can be observed even when the inclination is not close to 90°. But when the inclination is close to being 0°, the intensity of scattered light and the polarimetric values remain the same throughout the orbit due to the fact that α does not change for the observer. However, linear polarization still shows a rotation with sine-like variation of *Stokes* Q and U, which has same amplitudes but a phase shift of 90° (Fluri & Berdyugina 2010). Due to the geometry of orbital mechanics, under usual circumstances the degree of polarization reaches maximum when phase angle α is near 90° or 270° and touches minimum when it is near 0° or 180°. *By plotting observed polarimetric variations in Stokes Q and U over a period of time, the orbital period of an exoplanet can be deduced but a plot of single orbital period should demonstrate two peaks.*

A theoretical model predicted by Fluri and Berdyugina (2010) concluded: 1. The degree of polarization varies along with scattering angle ψ. Due to the geometry, it is maximum at 90° and minimum for backward and forward scattering angles. 2. At higher phase function ϕ, the polarization is larger as ϕ gives the fraction of incident light seen by the observer. At maximum phase function, the phase angle is the smallest. It means that when an orbiting planet is the farthest away from an observer then the phase function reaches its maximum with the smallest phase angle but when this planet is at its closest point to an observer then the phase function is at minimum with the largest phase angle. 3. In accordance with the incoming flux, the degree of polarization is inversely proportional to the square of distance D (the distance between host star and orbiting planet). For elliptical orbits, this distance D varies with the changing orbital phase. 4. A planets with larger radius has larger scattering surface and thus larger degree of polarization. 5. Linear polarization rotates as the planet orbits with a direction perpendicular to scattering's plane. Therefore, it results in exchange and change of signs for both *Stokes* Q and U.

2.2.2 Characterization

The characteristics of an exoplanet such as chemical compositions of the atmosphere, spatial distributions of atmospheric constituents and presence of oceans on the surface require direct observations. Due to the fact that faint signal of an exoplanet gets easily diluted in the bright stellar glare, the direction observations of exoplanets are extremely challenging. The use of polarimetry to a certain extent can help to overcome this challenge. Starlight is scattered by gas molecules, aerosol and/or cloud particles in the planetary atmosphere (if present) and reflected by the planetary surface (if the atmosphere is not optically thick). The outgoing radiation gets imprinted by each scattering particle present in the planetary atmosphere and it

affects the degree and position angle of polarization. Therefore, polarimetry of exoplanets is a very useful tool to facilitate the exoplanetary characterization.

The degree of polarization in reflected starlight depends on: *(i) the phase angle α, (ii) the atmospheric structure and composition of exoplanet, (iii) the reflection properties of the surface (if any) of exoplanet, (iv) The light wavelength λ and it does not depend on size of the exoplanet neither on its distance to the host star or to the observer.* (Stam 2013)

As scattering particles such as atomic or molecular gases are usually significantly smaller than the wavelength of incident light, *Rayleigh scattering* imparts a high degree of linear polarization. The polarization of light in the Rayleigh limit is:

$$P(\lambda, \psi) \propto sin^2\psi/(1 + \cos^2\psi). \tag{17}$$

The degree of polarization for scattered light is constant with λ but since Rayleigh-scattered light scales with λ^{-4}, polarization of the star–planet system has dependence on λ^{-4}. Therefore, linear polarization caused by scattering on molecules increases strongly towards blue and near ultra-violet (UV) wavelengths. Due to this fact, polarimetry in the blue and near UV passbands is required for possible detection of polarization in the case of exoplanets. Depending on the size of atmospheric particles, a simple geometric scattering or Mie scattering can also take place.

The equilibrium temperature of a planet is defined as the temperature of a black body whose emitted flux equals the incident flux from the host star at location of the planet. It has a huge impact on the composition of condensate particles present in its atmosphere. This influences the planet's geometric albedo and morphology of its phase function (Sudarsky et al. 2005). Equilibrium temperature is given as:

$$T_p = T_*(1 - A_B)^{1/4}\sqrt{R_*/2D}, \tag{18}$$

where T_p is planet's equilibrium temperature, T_* is the host star's effective temperature (temperature of a black body required to produce the known luminosity of the star with stellar radius R_*) and D is the planet to star distance. A_B is Bond Albedo that always ranges from 0 to 1. It can be described as the comparison of total radiation reflected by an object into space at all angles to the total incoming radiation the object received from the source. Bond Albedo is given by:

$$A_B = pq, \tag{19}$$

where p is geometric albedo, related to polarization as shown in Equation (15) and q is the phase integral given as:

$$q = \int_0^{\pi} \phi(\alpha) \sin \alpha d\alpha. \tag{20}$$

The planetary flux divided by the reflected flux for a perfectly diffusing disk with the same radius is known as geometric albedo. In case of a Lambert sphere where all incoming photons are scattered singly and isotropically: $p = 2/3$.

However, Lambert sphere approximation is not realistic for the actual observations. It is due to the fact that real situations are far more complicated and a number of factors can cause tiny variations of light. Firstly, the single scattering albedo $\tilde{\omega}$ is usually not the same due to the absorption of optical photons by gas or condensates in a given CEGP atmosphere. They either get re-emitted in the infrared wavelengths or cause a contribution to the thermal pool. Secondly, the chances of absorption in various types of scattering is higher than single scattering for the same single scattering albedo. Depending on mean free path of a photon, every scattering photon has a next encounter of a scattering probability of $\tilde{\omega}$. In case of absorption its contribution to scattering light does not occur. Thirdly, for smaller wavelength of light with respect to particles, these particles are more likely to forward scatter and enter the atmosphere. They are then often scattered further down into the atmosphere and are gradually absorbed instead of getting backscattered and escaping the planetary atmosphere. (Seager et al 2000)

Seager et al (2000) further derived certain geometric albedo values for particles of different sizes present in a planetary atmosphere as shown in Table 1. For very small particles with respect to the wavelength with mean radius $\bar{r} = 0.01\mu m$ at $i = 90°$, the quantity of light that gets scattered is very small because of high absorptivity in Fe and Al_2O_3. When the particles of $MgSiO_3$ are the only condensate available in the atmosphere without highly absorbing Fe and Al_2O_3, the fractional polarization should peak at 5.5×10^{-6}. It is almost 2 orders of higher magnitude than $MgSiO_3$-Fe-Al_2O_3 mix. In case of pure $MgSiO_3$ clouds for $\bar{r} = 0.1\mu m$ at $i = 90°$, equates to a geometric albedo $p = 0.69$ and peak value of fractional polarization is 8.6×10^{-5}. For particles $\bar{r} = 1\mu m$ and $\bar{r} = 10\mu m$, i.e., larger than the visual wavelengths, at $i = 90°$, the fractional polarization peaks at 3.7×10^{-6} and 7.5×10^{-6} respectively. A number of polarization peaks for various CEGP systems are shown in Figure 6.

Kedziora-Chudczer and Bailey (2010) concluded that polarimetry can help to detect oceans on the exoplanet. Even though oceans have very low albedo, they can

Table 1. Geometric Albedos.

Mean Particle Size	$\lambda = 5500$Å	$\lambda = 5500$Å ($MgSiO_3$)	$\lambda = 4800$Å
$0.01\mu m$	0.0013	0.18	0.0013
$0.1\mu m$	0.18	0.69	0.14
$1\mu m$	0.41	0.50	0.36
$10\mu m$	0.44	0.55	0.4

Geometric albedos for the models discussed in Seager et al (2000), $\lambda = 4800$Å(third column), corresponds to Cameron et al (1999) and Charbonneau et al (1999) observations.

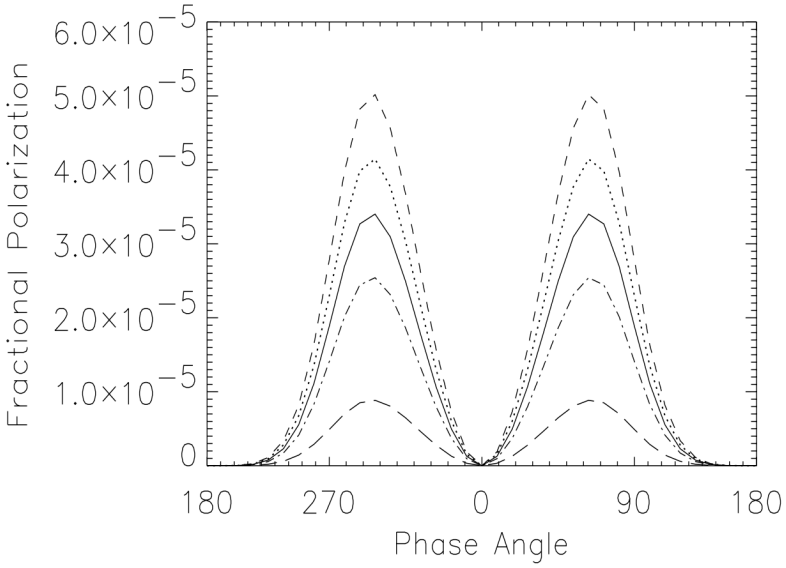

Figure 6. The degree of polarization curves for CEGP systems with different D and $R_p = 1.2R_j$, where R_p and R_j are radius of planet and radius of Jupiter respectively. In descending order the curves are for D = 0.042AU (HD 187123 b), D = 0.0462AU (τ Boo b), D = 0.051AU (51 Peg b), D = 0.059AU (υ And b) and D = 0.11AU (55 Cnc b). Image from Seager et al (2000).

reflect the incident light like a mirror. This phenomenon can be referred as specular reflection or glint and such light is highly polarized. If an exoplanet has a natural satellite (*exomoon*), it can affect glint polarization that should peak at crescent phases. The degree of polarization can be very high for an exoplanet totally covered by ocean. Clouds in an exoplanet atmosphere can polarize the starlight too, and the degree of such polarization depends on their chemical composition. By using polarimetry, it has been figured out that clouds in the atmosphere of Venus are 75% H_2SO_4 and 25% H_2O (Hansen and Hovenier 1974).

2.3 Stellar Polarization

The most common factors that can contribute to the degree of polarization of any astronomical object are instrumental polarization and interstellar polarization. However, these factors are always considered and accounted for whenever polarimetric observations are interpreted. But when interpreting polarimetric observations of exoplanets, polarization arising from stellar activity of host stars should also be considered.

A few decades ago when the accuracy of polarimeters was not as high, astronomers thought that simply building polarimeters with high precision capabilities would be enough to detect and interpret polarimetric signals from exoplanets. However, once such polarimeters were built and utilized, it turned out that stellar activity in the host stars can contaminate the polarization signal from exoplanets (e.g. Berdyugina et al 2011). Therefore, whenever observing polarization of an exoplanet that is hosted by a star with magnetic activity or starspots, the stellar polarization should be taken into account.

Two main causes of intrinsic stellar polarization are: (i) Zeeman effect due to magnetic fields of moderate strengths cause spectral lines split into polarized components of equal strength but with opposite polarization. When observed with the broadband filter, this type of polarization is canceled out. Therefore, the usual polarimetric measurements of exoplanets do not get affected. (ii) If there are spots on the stellar surface, which is a quite common occurrence, the polarization from scattering is not equally canceled out over the visible stellar disk. It results in a residual polarization due to Rayleigh scattering in the atmosphere of host star and thus contributes to broadband polarimetric measurements of exoplanets. (Kostogryz & Berdyugina 2015; Kostogryz et al 2016; Yakobchuk & Berdyugina 2018)

The polarization caused by starspots results in vertical offsets in the polarization

curves. It can change the degree of variations even for non transiting exoplanets. These starspots are barely detectable in the light curves of relative flux. The parameters of polarization depend on spot sizes, location and therefore are able to reveal stellar rotation period. The integral polarized light is sensitive to various locations of starspots. It is quite evident that near-limb starspot can contribute higher to the degree of polarization than starspot at any other location. When superimpose, the degree of polarization arising from both starspots and the planets can compensate each other. The maximum compensation for *Stokes* q and u parameters can be observed when the angle between aplanet and the starspot is $\pm 90^{\circ}$ as seen from the center of stellar disk. It becomes particularly significant when many starspots are present on a stellar surface. (Kostogryz at al 2015)

In principle, polarimetry of exoplanets not just help deduce orbital and physical properties of planets but also reveals stellar characteristics of the host stars. For a star that exhibits polarization due to starspots, the degree of polarization only depends on the rotation axis inclination angle. It varies according to aspect and location of the spot and thus lined with stellar rotation. In this scenario, the degree of stellar polarization is given as:

$$p(\psi) = \frac{I_p(\psi)}{I_{\text{tot}}(\psi)} = \frac{\sin^2 \psi}{1 + \cos^2 \psi}, \tag{21}$$

where I_p is polarized flux, I_{tot} is total flux and ψ is scattering angle. Clarke (2003) deduced that any cyclic phenomenon including non-radial pulsations that causes non-sinusoidal type of variations with forms dependent on the parameter to be measured. It will result in periodograms containing fundamental period and harmonics. Therefore, it is highly possible to have integer sub-multiples of the stellar rotational period when visualizing such polarimetric data.

Yakobchuk and Berdyugina (2018) concluded that linear polarization due to starspots has typical values between 10^{-6} and 10^{-4}. This can produce a signal that is a mixture of polarizations caused by the exoplanet and starspots. It can be challenging to separate these two polarizations due to the fact that at the time of writing this text, no theoretical model has been developed that can help distinguish between stellar and planetary polarization of distant stars. Another problem is the separation of these two polarizations due to closeness of the orbital period of exoplanet and the rotational period or sub-multiples of the rotational period of the host star.

Table 2. Orbital and physical parameters of υ And b.

Parameter	Butler et al (2006)	McArthur et al (2010)	Curiel et al (2011)	Berdyugina et al (2011)
P [days]	4.61711(8)	4.61711(1)	4.61703(3)	4.61711
T_p^1	1802.6(7)	...	...	32.451(1)[2]
T_t^1	1802.97(3)	34.1(3)	5.37(5)	34.668(1)[2]
P [AU]	0.060(3)	0.0594(3)	0.0592217(2)	0.0594
e	0.02(2)	0.012(5)	0.0215(7)	0.012
i [deg]	...	...	...	111(11)
ω [deg]	63(?)	44(26)	325(4)	279(14)
Ω [deg]	...	...	...	236(12)
$M/M_J \sin i$	0.69(6)	0.69(2)	0.688(4)	...
M/M_J	...	...	...	0.74(7)
R_{RL}/R_J	...	...	...	1.36(20)
ρ [gcm^{-3}]	...	...	...	0.36(8)
g [10^3cms^{-2}]	...	...	...	0.99(46)

[1]JD 2,45,000+, [2]T_p = 1800.805 and 4.749, T_t = 1803.021 and 6.965 to compare with Butler et al (2006), Curiel et al (2011) respectively and Ω can also be 56° due to the 180° ambiguity.

2.4 Upsilon Andromedae b

Upsilon Andromedae b (υ And b) is an innermost exoplanet in the planetary system of the bright star ($m_V = 4.10$) Upsilon Andromedae. This exoplanet can be categorized as CEGP, as it orbits its host star with an orbital period of just about 4.6 days and has a lower mass limit of about 0.74M$_\mathrm{J}$ (Berdyugina et al 2011), where M$_\mathrm{J}$ is the mass of Jupiter. It is one of the earliest discovered exoplanets detected using Doppler spectroscopy. The host star is an F8 dwarf and hosts another three exoplanets (McArthur et al 2010). The υ And b is one of the exceptional exoplanets that has been directly detected in the infrared wavelengths. It is a non-transiting exoplanet and thus polarimetry can potentially reveal details which are not possible to study with other observational techniques. Thus, υ And b has been considered as one of the most promising targets, expected to show significantly strong degree of polarization due to Rayleigh scattering. The geometric albedo of υ And b is estimated to be 0.53±0.27 for 345–388nm, 0.67±0.24 for 390–490nm and 0.29±0.23 for 500–490nm (Berdyugina et al 2011). The analysis of Hipparcos photometry data collected for υ And b has revealed that the host star has a rotational period of 7.88 days (Berdyugina et al 2011), which is visible possibly due to the starspots caused by magnetic activity.

In 2016 - 2019, υ And b has been observed for more than one hundred nights with the Dipol-2 polarimeter on the 60cm remotely controlled Tohoku telescope at Haleakalā

Observatory (Hawaii). The following chapter gives description of the instrument, as well as the data collection and calibration procedures. In final chapter, this study presents the results of polarization data analysis and compare them with already available information on υ And b that is shown in Table 2.

3 Polarimetric Observations

The polarimetric observations analyzed in this study were observed on Tohoku 60cm telescope (T60) with DiPol-2 polarimeter. T60 is owned by University of Tohoku, Japan and it is presently installed at Haleakalā Observatory on Maui Island, Hawaii. DiPol-2 is a double-image high precision polarimeter, jointly developed by Finnish Center for Astronomy with the ESO (FINCA), University of Turku and Leibniz Institute for Solar Physics, Freiburg, Germany. The DiPol-2 polarimeter on the T60 is mainly used for observations of interstellar polarization, interacting early-type binaries and stars with exoplanets. Both T60 and DiPol-2 can be operated remotely (via Internet) from any place, including Finland.

3.1 The Telescope

T60, as the name suggests, uses a 60cm primary mirror. It has the Cassegrain two-mirrors design, where the incoming light is first reflected by a large concave paraboloid mirror and then onto a smaller convex hyperboloid mirror, which is then reflected again through a hole within the large mirror in order to form an image (see Figure 7). The advantages of this design is that it puts the focal point behind the primary mirror at a convenient location. This helps secondary mirror to add a telephoto effect that creates a much longer focal length within this compact system. This makes it an excellent option for astronomical purposes such as deep sky viewing, planetary and lunar observations. Telescope of Cassegrain type is also the best option for

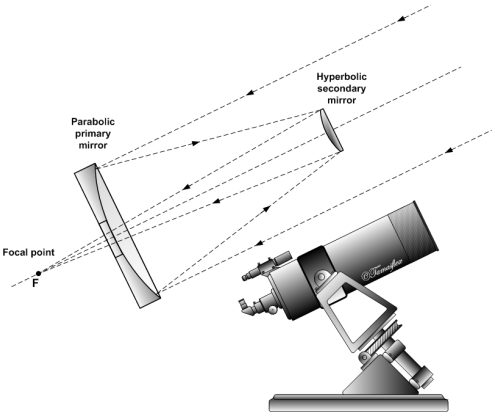

Figure 7. An illustration of the light path in Cassegrain telescope such as T60. Image from Szőcs Tamás, tamasflex, (2009).

the high-precision polarimetry, because perfectly symmetric reflections minimize instrumental polarization.

The telescope has been in operation since 1999. It was first installed at Iitate Observatory in Fukushima, Japan. After the earthquake in 2011, a decision to relocate the telescope to Hawaii has been made. It resumed its operation on Haleakala Observatory in September 2014. The Haleakalā summit (3050 m) located on Maui Island, is one of the finest sites for astronomical observations on the planet. This site benefits from clear skies, good seeing conditions and low humidity. T60 is also used for observations of atmospheres of Solar system planets in the infrared by using Infrared Heterodyne Spectrometer (MIRAHI). There is also a high-dispersion spectrometer with coronagraph which is used for observations of Jupiter and Jovian moons. The optical polarimeter DiPol-2 has been installed at T60 in December 2014.

3.2 The Polarimeter

The layout of the DiPol-2 polarimeter is shown on Figure 8. It uses two dichroic beam-splitters which split incident light beam into the B, V and R passbands which are simultaneously recorded by three CCD cameras. The polarization modulator is a discretely rotatable superachromatic $\lambda/2$ (or $\lambda/4$) plate and polarization analyzer is a plane parallel calcite plate. The use of a superachromatic wave plate enables measurements of polarization in a wide spectral range from 400nm to 800nm. A typical cycle of polarimetric measurement consists of 16 exposures at the orientation intervals of 22.5° for linear polarization or $4 \times 90°$ for circular polarization. The calcite plate produces two orthogonally polarized stellar images that are recorded simultaneously in order to eliminate errors which may arise due to changing in atmospheric transparency. Because of the *parallel* image splitting in the calcite plate,

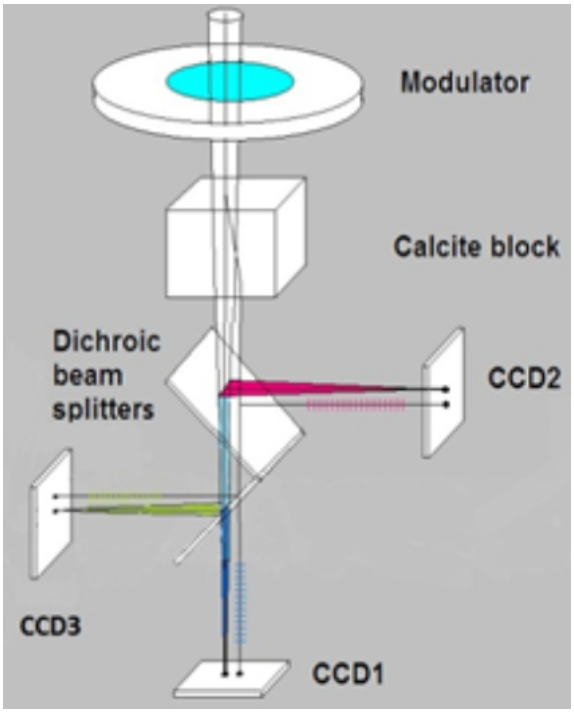

Figure 8. Layout of DiPol-2, showing components of the polarimeter. Image from Piirola et al (2014).

two orthogonally polarized images of the background sky are overlaid, and thus the contribution from the sky polarization is automatically canceled out. DiPol-2 is capable to measure polarization at the precision better than 10^{-5}. Polarimeter control and data acquisition is done with the single industrial-grade compact computer that contains three USB and one COM ports. The polarimeter has been designed for the remote observations. In total, three copies of DiPol-2 have been manufactured till to date, including the one that is installed at the T60 right now.

3.3 Observations

Most observing nights used for polarimetry at T60 telescope are shared with the coronograph which is used by astronomers from Planetary Plasma and Atmospheric Research Center at Tohoku University. Both instruments are mounted on the motorized slide installed in the Cassegrain focus. Instrument change can be done remotely at any time and takes less than 5 minutes. This allows to share telescope time between different observing programs very efficiently and helps to collect large amount of polarization data. Because the time difference between Hawaii and Finland is 12 hours, all remote polarimetric observations with the DiPol-2 are done in daytime. The observer opens connection to the two host computers located in the T60 control room via remote control software (VNC Viewer). One of these computers is used for operation of the telescope, and another one - for polarimeter control.

3.3.1 Telescope Control

Figure 9 shows the control panel of T60 Server program, which is open on the control computer running on Windows 7. This program provides full control over the telescope operation, such as: dome opening and closure; instrument exchange; telescope pointing, focusing and parking after the end of observing night. Automated weather station doesn't allow telescope opening at bad weather condition and closes it automatically, if the conditions become bad during observing session. The telescope is using DiPol-2 V-band CCD camera images for simultaneous auto-guiding.

3.3.2 DiPol-2 Control

The desktop of DiPol-2 control computer is shown on Figure 10. For observations, two pieces of software: MaxIM DL Pro and CCDSoft are used. MaxIM DL Pro is responsible for control and data acquisition in the B and R passbands, and CCDSoft in the V passband. Data are collected by the three CCD cameras simultaneously. The field of view for the B-band image (Apogee Alta U47, thinned, back-illuminated,

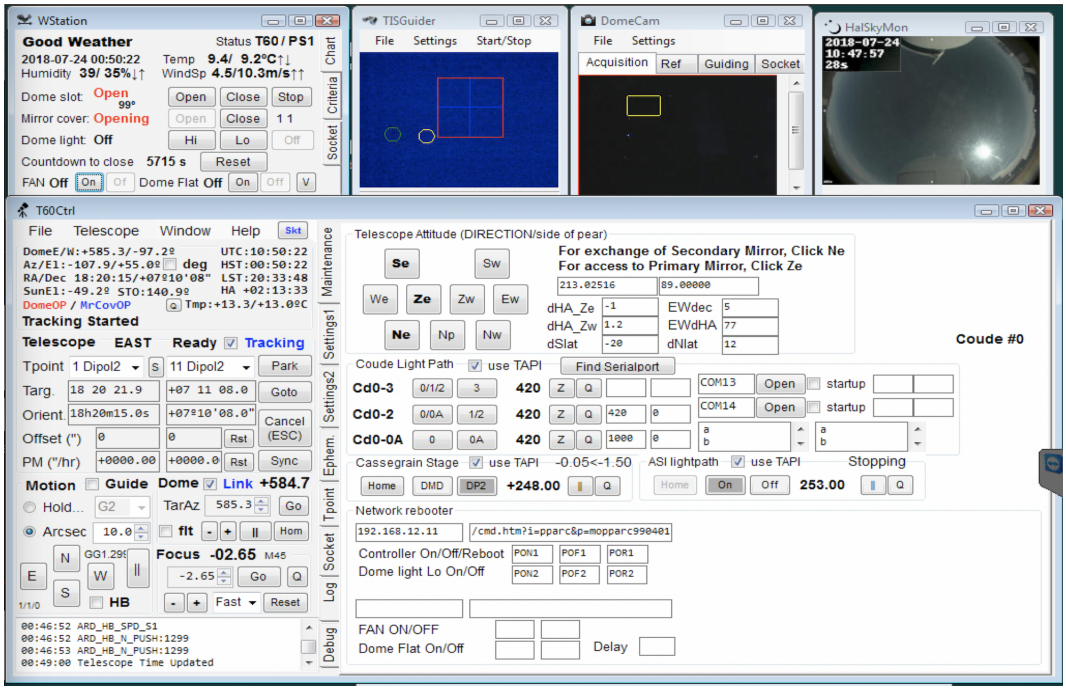

Figure 9. A screen shot of the control panel of T60Server. It shows a number of panels that are used to perform observations.

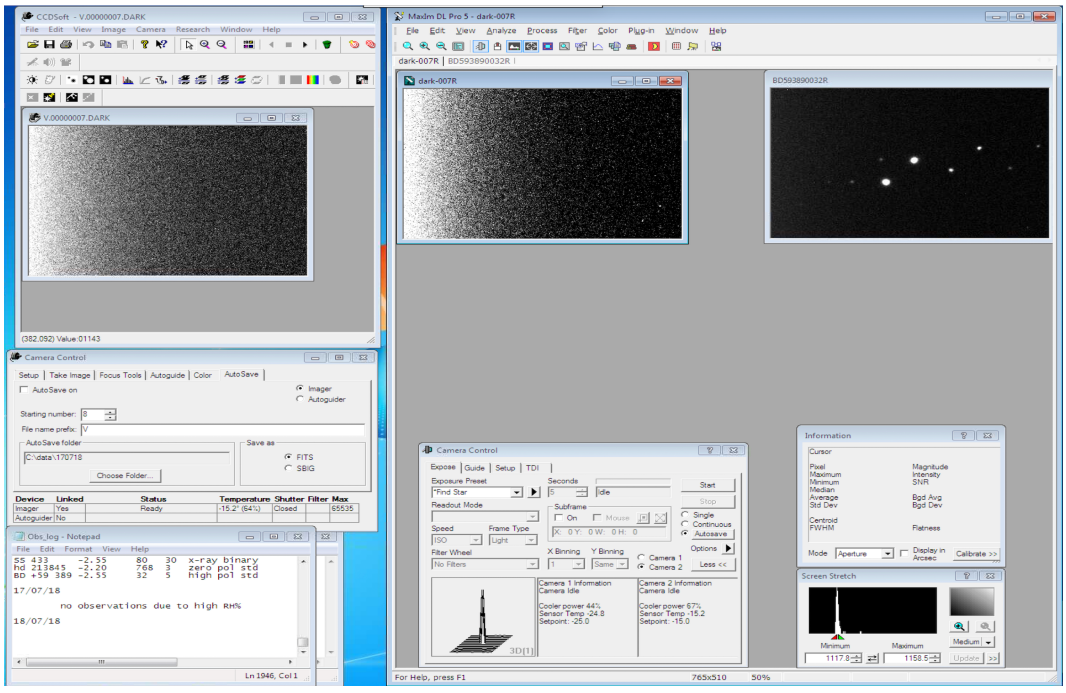

Figure 10. A screen shot of DiPol-2 computer during an observation. MaxIM DL Pro is used to take observations in B and R passbands while CCDSoft is used for V passband. Notepad is used to keep observation log and edit Visual Basic scripts.

1024 x 1024, pixel size = 15 x 15 μm) has the size of $\sim$7 arcsec, while for the V and R-bands (SBIG ST-402ME, 765 x 510, pixel size = 9 x 9 μm) it is $\sim$3.0 x 2.5 arcsec. The exposure time for the each CCD camera can be set individually. The camera exposures are synchronized with the rotation of the wave plate which is done by the stepper motor. The total image download time is $\leq$ 2 sec.

3.3.3 Observations of Upsilon Andromedae

The υ And was observed with the DiPol-2 and T60 in the period from 24 October, 2016 to 15 January, 2019. At the Haleakalā summit, υ And is well visible from September through March. The observational data for a total of 114 nights were eventually good enough to be used for follow up data analysis. The observational data for the few nights were discarded due to the bad quality that was either caused by poor visibility (clouds) or bad seeing. Skyflat images that are used for calibration purposes have been regularly taken at the time of twilight hours that is either in the beginning of observing night or at the dawn. Once per night, the series of dark and bias images have been always taken.

The star system of υ And is a bright target with an apparent magnitude of 4.60 and thus visible to human eye. In order to avoid pixel saturation and yet collect sufficient amount of ADUs, DiPol-2 employs the "intentional defocusing" technique. By defocusing, the stellar image is spread over the large number of pixels. Normally, around of 768 – 832 images have been taken every night with the exposure time of 2 – 3 s. This corresponds to 256 – 260 measurements of Stokes q and u per night. Then, the weighted average value of Stokes parameters has been computed. The resulting accuracy is at the level of $1 - 2 \times 10^{-5}$ in the B-band and even better $(0.7 - 1.5 \times 10^{-5})$ in the V and R-bands (see Figure 11).

To subtract instrumental polarization and determine a zero-point of polarization angle, zero polarization and high polarization standard stars are regularly observed.

3.4 Data Reduction

The observational data obtained for υ And were initially stored at the DiPol-2 computer. They have been then transferred to the office computer in the Department of Physics and Astronomy at University of Turku. The data set for 114 nights consists of about 300,000 image files.

Figure 11. Defocused CCD images of images of υ And in the B = 4400Å(left), V = 5500Å(center) and R = 7000Å(right) passbands. The faint "stars" visible on the V and R images are the reflections produced by dichroic beam splitters. They appear bright due to exaggerated contrast. In fact, the total intensity of reflection is $< 0.1\%$ of that produced by stellar image.

3.4.1 Calibration of Raw CCD Images

In astronomical images, raw observational frames contain some imperfections that must be removed before using these frames for scientific studies. The observational images can include bias signal, hot pixels, thermal noise, vignetting and dust. By subtracting bias and dark frames and applying flat fielding, the spurious effects arising from these imperfections can be eliminated. This is done via automated Visual Basic scripts that are capable to process several hundreds of polarimetry CCD images simultaneously. A special algorithm has been developed to remove possible effect of the image drift to pre-align images taken in long series of polarimetric sequences. The scripts, executed with the MaxIM DL Pro, perform the calibration and create 2 x 2 binned sub-frames for every taken raw image.

3.4.2 Flux Extraction and Computation of Polarization Parameters

Normalized Stokes parameters q and u are computed from the flux intensity ratios of the orthogonally polarized stellar images $Q_i = I_e(i)/I_o(i)$ obtained for the each orientation of wave plate $i = 0.0°$, $22.5°$, $45.0°$, $67.5°$ as:

$$\begin{aligned} Q_m &= Q_{0.0} + Q_{22.5} + Q_{45.0} + Q_{67.5}, \\ q &= (Q_{0.0} - Q_{45.0})/Q_m, \\ u &= (Q_{22.5} - Q_{67.5})/Q_m. \end{aligned} \tag{22}$$

The intensities $I_e(i)$ and $I_o(i)$ have been determined from the series of calibrated polarimetry images with the *aperture photometry method* implemented as the standard feature in the MaxIM DL Pro software. Simple Fortran code is used to compute the

J.D.	Px	(%)	Py	P	(%)	m.e.	P.A.	m.e	N	Nw	file	No
58025.924	-0.0006		0.0007	0.0010	0.00112		66.5	24.8	224	4%	upsan	101
58026.928	-0.0000		-0.0043	0.0043	0.00162		134.8	10.3	208	10%	upsan	102
58027.948	0.0003		-0.0038	0.0038	0.00290		137.1	18.6	224	17%	upsan	103
58029.012	-0.0030		-0.0005	0.0030	0.00125		94.6	11.2	208	8%	upsan	104
58029.907	-0.0008		-0.0021	0.0022	0.00175		124.9	19.2	224	10%	upsan	105
58032.002	-0.0011		-0.0031	0.0033	0.00179		125.1	14.2	192	7%	upsan	106
58032.916	-0.0005		-0.0034	0.0034	0.00249		131.1	18.2	213	14%	upsan	107
58033.911	-0.0018		-0.0001	0.0018	0.00123		91.2	17.3	224	8%	upsan	108
58034.950	-0.0021		0.0004	0.0021	0.00284		84.1	26.5	240	20%	upsan	109
58036.962	-0.0003		-0.0006	0.0007	0.00138		123.7	31.7	224	14%	upsan	110
58037.942	-0.0005		-0.0003	0.0006	0.00116		103.6	31.6	240	8%	upsan	111
58044.895	0.0008		-0.0029	0.0030	0.00120		142.8	10.8	200	8%	upsan	112
58045.888	-0.0026		-0.0021	0.0033	0.00106		109.2	8.9	224	4%	upsan	113
58053.863	-0.0029		-0.0015	0.0033	0.00112		103.4	9.5	224	8%	upsan	114
58054.916	-0.0021		-0.0026	0.0034	0.00112		115.5	9.2	224	7%	upsan	115
58055.903	-0.0005		-0.0006	0.0008	0.00110		116.6	27.5	208	5%	upsan	116
58056.870	-0.0012		-0.0012	0.0017	0.00123		112.1	17.9	208	8%	upsan	117
58059.891	-0.0041		-0.0001	0.0041	0.00136		90.6	9.1	224	16%	upsan	118
58060.898	-0.0012		-0.0027	0.0030	0.00102		123.2	9.5	216	2%	upsan	119
58062.911	-0.0001		-0.0004	0.0004	0.00122		126.9	36.6	208	6%	upsan	120
58063.872	-0.0004		-0.0039	0.0039	0.00115		131.7	8.2	192	4%	upsan	121
58064.860	-0.0017		-0.0026	0.0031	0.00111		118.6	10.0	216	5%	upsan	122
58065.911	0.0002		-0.0010	0.0010	0.00112		140.5	23.9	208	4%	upsan	123
58066.825	-0.0028		-0.0001	0.0028	0.00113		90.9	10.9	208	4%	upsan	124
58067.895	0.0007		-0.0017	0.0018	0.00127		146.5	17.5	208	8%	upsan	125

Figure 12. A printout of Fortran code. Here the designations "Px" and "Py" are used for Stokes q and u. The value of Julian date is also computed. The errors of the weighted average values of polarization (P) and polarization angle (P.A.) are designated as "m.e".

Stokes parameters q and u from each set of four images. This code can also compute the *weighted average* values of polarization. It gives lower weight to individual measurements of *Stokes* q and u that deviate from the mean value by more than expected from Gaussian noise distribution. All measurement points which deviate less than 2σ are given equal weight. Any points with deviation more than 2σ are weighted according to $G = (\sigma/s)^2$, where σ is the standard deviation of the distribution and s increases linearly from 1σ to 3σ. Any points deviating more than 3σ are rejected. Using Stokes parameters q and u, code computes the values of polarization P and polarization angle θ. It also outputs the value of Nw (see Figure 12), which is the percentage of data points to which the weighting is applied. In normal conditions $Nw = 6 - 8\%$, but it can be higher in case of a cloudy night or any other situation affecting the image quality.

3.4.3 Instrumental Polarization

The instrumental polarization has been derived from observations of 20 – 25 zero-polarized standard stars. It was found to be in the range of $4 - 6 \times 10^{-5}$. The accuracy of determination of instrumental polarization for the DiPol-2 is $2 - 3 \times 10^{-6}$.

Polarization values for υ And have been corrected for instrumental polariziton. This is done with another Fortran program which also corrects the polarization angle taking into account the angle zero-point, determined from observations of two highly polarized standard stars. The resultant values could then be used for data analysis.

In principle, for determination of the *intrinsic* polarization of the distant object, the Interstellar polarization should be somehow measured and subtracted. It is normally done by observing a few objects in vicinity of the target. However, because υ And is located at the distance of only 13.5 pc from the Sun, the contribution from the interstellar polarization component must be absolutely negligible.

4 Data Analysis

To interpret measurements taken from the observations, data analysis is performed. Due to huge volumes of astronomical data, the analysis requires highly efficient computers. Python has become one of the most popular computer programming languages for astronomical data analysis. In the field of observational astronomy, an efficient algorithm to detect and characterize periodic signals in unevenly sampled data is of immense importance for the data analysis. Lomb–Scargle periodogram algorithm is often used with astronomical data for the purpose of period detection. In this algorithm, noise is chi-square distributed at each individual frequency to produce a periodogram that is equivalent to a periodogram derived from the least squares analysis.

Curve fitting is a useful technique to visualize astronomical data, which helps to deduct values of a function where no data is available. The process of constructing a curve requires the best fit to a series of data points that either exactly fits the data or a function is constructed to approximately fit the data. In curve fitting, a certain degree of uncertainty is always present as it is performed beyond the range of available data or in the intervals with no data. Fourier series curve fitting is often used for asymmetric periodic curves as often present in polarimetric data. For the analysis of υ And data, several scripts were written in Python to generate Lomb-Scargle periodograms and MatLab was used to compute Fourier coefficients in order to perform curve fitting to the observational data.

4.1 Lomb-Scargle Periodogram

Lomb-Scargle periodogram uses the algorithm of least squares to fit sinusoids on data samples. The algorithm is closely related to Fourier analysis but it has the advantage to fit unevenly spaced data such as polarimetric data. In 1969, Petr Vaníček proposed *successive spectral analysis* with a result of *least-squares periodogram* for both evenly and unevenly spaced data. Initially, the algorithm only considered simple mean but later on the method was refined to include systematic components such as linear,

quadratic or exponential. Nicholas Lomb further simplified the method and figured out the closeness to periodogram analysis. Jeffrey Scargle showed that by slightly modifying the algorithm, this method becomes quite similar to Lomb's least-squares formula to fit individual sinusoid frequencies.

In non-linear least-squares fit, a set of m observations is fitted with a non-linear model that consists of n unknown parameters ($m \geq n$). The main task for this method is to define an objective function. Input values of fitting variables are given to this objective function that determine either a scalar value or array of values to be minimized. For astronomical data, later approach is mostly used in which objective function returns an array that is often scaled by using a weighting factor such as inverse of the uncertainty in data set. To do this, chi-square (χ^2) statistic is used and it is often defined as:

$$\chi^2 = \sum_i^N \frac{[y_i^{\text{obs}} - y_i^{\text{model}}(\mathbf{v})]^2}{\epsilon_i^2}, \tag{23}$$

where y_i^{obs} is the set of observed data, $y_i^{\text{model}}(\mathbf{v})$ is the model calculation, $\mathbf{v}$ is the set of input variables for the model to be optimized in the fit and ϵ_i are uncertainties in the data set. In a typical non-linear fit, an objective function is written in such a way that it takes input variables to either calculate the residual array $y_i^{\text{obs}} - y_i^{\text{model}}(\mathbf{v})$ or the residual array is scaled by the data uncertainties $[y_i^{\text{obs}} - y_i^{\text{model}}(\mathbf{v})]/\epsilon_i$ or by any other given weighting factor.

4.1.1 Lomb-Scargle Power

For data $[y_k]$ pre-centered such that $\Sigma_k y_k = 0$, the power $P(\omega)$ of Lomb-Scargle periodogram at frequency ω is estimated as:

$$P(\omega) = \frac{1}{2}\left(\frac{[\Sigma_k X_k \cos\omega(t_k - \tau)]^2}{\Sigma_k \cos^2\omega(t_k - \tau)} + \frac{[\Sigma_k X_k \sin\omega(t_k - \tau)]^2}{\Sigma_k \sin^2\omega(t_k - \tau)}\right), \tag{24}$$

where τ is time-offset, it orthogonalizes the model in order to make $P(\omega)$ independent of a translation in t that can be computed as:

$$\tan(2\omega\tau) = \frac{\Sigma_k \sin(2\omega t_k)}{\Sigma_k \cos(2\omega t_k)}. \tag{25}$$

For any given single frequency ω, the power given by the method is same as power given by the least-squares fitting to sinusoids of that particular frequency:

$$\phi(t) = A\sin(\omega t) + B\cos(\omega t). \tag{26}$$

Lomb–Scargle periodogram is valid for a model with zero mean. This is usually achieved by subtracting mean of the given data before the calculation of periodogram. In case of a model with non-zero mean, a constant off set is included:

$$\phi(t) = A\sin(\omega t) + B\cos(\omega t) + C. \tag{27}$$

In Lomb-Scargle periodogram, for any given frequency ω, the power is an $O(N)$ computation. This computation involves simple trigonometric sums over the data in which N denotes number of data points and notation O means *proportional to*.

4.1.2 Lomb-Scargle Frequencies

An important computational consideration to compute Lomb-Scargle periodogram is to choose number of frequencies. If one chooses a fine grid, it will result in excess computations that are otherwise not required. In case of a coarse grid, the peak of periodogram may fall down between the grid points.

Let us consider a candidate frequency f, data with range $T = t_{\max} - t_{\min}$ contains $T{\cdot}f$ complete cycles. The error in frequency δf, makes $T{\cdot}\delta f$ the error in number of cycles between the endpoints of data. However, the error should not be significant fraction of a cycle. As in such a case, it may significantly affect the fit and this can result in a grid-spacing criterion of $T{\cdot}\delta f \ll 1$. Frequency grid spacing can be described is: $T{\cdot}\delta f = (5T)^{-1}$, where 5 is chosen as an oversampling factor.

The frequency grid is also given lower and upper frequency limits. Due to numerical problems of choosing $f = 0$, minimum frequency is chosen to be δf. For irregularly sampled time-series data, the maximum frequency is determined based on the type of signal that is being searched for. It should base on prior knowledge of data or an intuition than any statistical rule. However, in many situations a commonly used maximum frequency is referred as *average* Nyquist frequency:

$$\hat{f}_{\mathrm{Ny}} = \frac{N}{2T}. \tag{28}$$

This will result in "typical" number of frequencies, i.e., the number of frequencies to investigate is scaled with number of data points:

$$N_{\text{freq}} \sim O\left(\frac{\hat{f}_{\text{Ny}}}{\delta f}\right) \sim \frac{N/(2T)}{1/T} \sim O(N). \tag{29}$$

Equation (29) shows that to get optimal value of Lomb-Scargle period within N data points, the computation of $O(N)$ expressions is required for power across $O(N)$ grid points. This makes Lomb-Scargle an $O(N^2)$ algorithm. In 1989, Press and Rybicki proposed an intelligent fast Fourier transform (FFT) for equally spaced data that is used on a grid extrapolated from the input data so that $O(N^2)$ problem can be computed in the same time that is required for $O(N \log N)$. This means that the resultant sum of cosines and sines of a single frequency also gives some details on the sum of another frequency. This information is used over a frequency grid to minimize the number of operations required. In Python, the Lomb-Scargle periodogram can be computed by either using $O(N^2)$ algorithm or $O(N \log N)$ algorithm.

4.2 Curve Fitting

Curve fitting is based on the assumption that a certain mathematical relationship is present between the quantities being related by the curve. Astronomical data points are never complete on a plot due to limited time slots available to observe any astronomical object. Thus curve fitting is often essential to visualize the missing data points in order to deduce any related characteristics to a particular data set. A curve can be drawn between different quantities by predicting a certain relationship, which can range from basic constant, linear, quadratic to advanced n^{th} order of polynomials. The most common curves that appear in astronomical data are *periodic*, i.e., the interval of two matching points in the plot. It basically means the measure of distance that the function travels along x-axis before repeating this very pattern. The basic sine and cosine functions contain a period of 2π and tangent contains a period of π. A simple sine function is given as:

$$y = A \sin(Bx + C), \tag{30}$$

where A is amplitude, B is number of cycles that the graph completes in an interval from 0 to 2π and C is phase shift.

However, in most cases that involve polarimetric data, the curves are not basic sinusoidal but instead asymmetric sine curves due to spherical harmonics. More complex periodic functions can be analyzed into their constituent components both

fundamentals and harmonics by *Fourier analysis*, the origin of Fourier transform. The Fourier series processes a periodic signal $x(t)$ as a sum of sine and cosine waves. Since sine and cosine are periodic functions, the resultant $x(t)$ will also be a periodic function:

$$x(t) = x(t + nT),\ n \in \mathbb{Z}. \tag{31}$$

Fourier series of $x(t)$ can be written as:

$$x(t) = \frac{a_0}{2} + \sum_{n=1}^{\infty} \left[a_n \cos\left(\frac{2\pi nt}{T}\right) + b_n \sin\left(\frac{2\pi nt}{T}\right) \right], \tag{32}$$

where T is period, a_0, a_n and b_n are Fourier coefficients and defined by the following integrals:

$$\begin{aligned} a_0 &= \frac{1}{T}\int_0^T x(t)dt, \\ a_n &= \frac{2}{T}\int_0^T x(t)\cos\left(\frac{2\pi nt}{T}\right)dt, \\ b_n &= \frac{2}{T}\int_0^T x(t)\sin\left(\frac{2\pi nt}{T}\right)dt, \end{aligned} \tag{33}$$

where $\frac{1}{T}, \frac{2}{T}, \frac{3}{T}, ...$, are frequencies of the sines and cosines, i.e., multiples of the fundamental frequency $\frac{1}{T}$. They are inverse period duration of the function in which frequency $\frac{n}{T}$ is called the n^{th} harmonic.

4.3 Period Analysis of Upsilon Andromedae b

A number of scripts based on Lomb-Scargle periodogram algorithm were written to analyze polarimetric measurements of υ And. In Python, *gatspy.periodic* implementation of Lomb-Scargle was used that is based on $O(N \log N)$ algorithm. The data was arranged in six different files based on *Stokes* q and u in B, V and R passbands. The oversampling factor was set at 5000 as it turned out to be the best compromised value between optimal results and computational time. Since the main purpose was to look for orbital period of exoplanet, a reasonable limit of between 1.5 to 7.5 days was set as the range of grid. The period range was given in days instead of frequencies by using *optimizer.period_range* in *periodic.LombScargle* implementation of Python.

The main script was coded to find out the values of five highest peaks and print them on the periodogram. It was expected that power of Lomb-Scargle peaks would be quite low and it becme evident by periodograms in Figures 13-18, where Lomb-Scargle power on y-axis was chosen from 0 to 0.15 instead of standard 0 to 1. This is due to the nature of data where the variability in Stokes q and u parameters is very small as compared to the measuring errors, i.e., $\Delta(q, u) \approx \sigma(q, u)$.

To visualize Lomb-Scargle periodograms, curve fitting was performed on data points by selecting the highest peak between the orbital period of 2.0 to 3.0 days. This range is chosen due to the fact that degree of polarization varies along the phase angle and shows two peaks in a single orbit. Therefore, the known orbital period of υ And b that is $\sim$4.6 days should show a Lomb-Scargle peak at $\sim$2.3 days. The data is phase folded for the highest Lomb-Scargle peak related to the planetary orbital peak at $\sim$2.3 days.

The polarimetric curves depend on a number of factors such as the scattering particle size or type, scattering albedo and the atmospheric density. Second harmonics may appear if there is asymmetry in distribution of light scattering material about the orbital plane. Brown et al (1978) and Rudy & Kemp (1978) studied the polarization caused by Thomson scattering in circumstellar envelopes of binary systems. Their conclusion was that for the observed phase-resolved curves of Stokes parameters q and u are best fitted with a truncated first and second order Fourier series:

$$\begin{aligned} q &= q_0 + q_1 \cos(\lambda) + q_2 \sin(\lambda) + q_3 \cos(2\lambda) + q_4 \sin(2\lambda), \\ u &= u_0 + u_1 \cos(\lambda) + u_2 \sin(\lambda) + u_3 \cos(2\lambda) + u_4 \sin(2\lambda), \end{aligned} \tag{34}$$

where $\lambda = 2\pi\phi$ is orbital longitude and ϕ is the orbital phase ($0 < \phi < 1$), while q_0, q_1, q_2, q_3, q_4, and u_0, u_1, u_2, u_3, u_4 are coefficients. These coefficients of the fit can also be used to deduce the value of orbital inclination. It is expected that usually the second order variations should dominate:

$$\left[\frac{1 - \cos i}{1 + \cos i}\right]^4 = \frac{(u_3 + q_4)^2 + (u_4 - q_3)^2}{(u_4 + q_3)^2 + (u_3 - q_4)^2}. \tag{35}$$

In curve fitting plots of Figures 13-18, x-axis is the phase of each observation instead of the observation time. Equation (34) was used to do the curve fitting plots as Fourier coefficients were computed using MatLab.

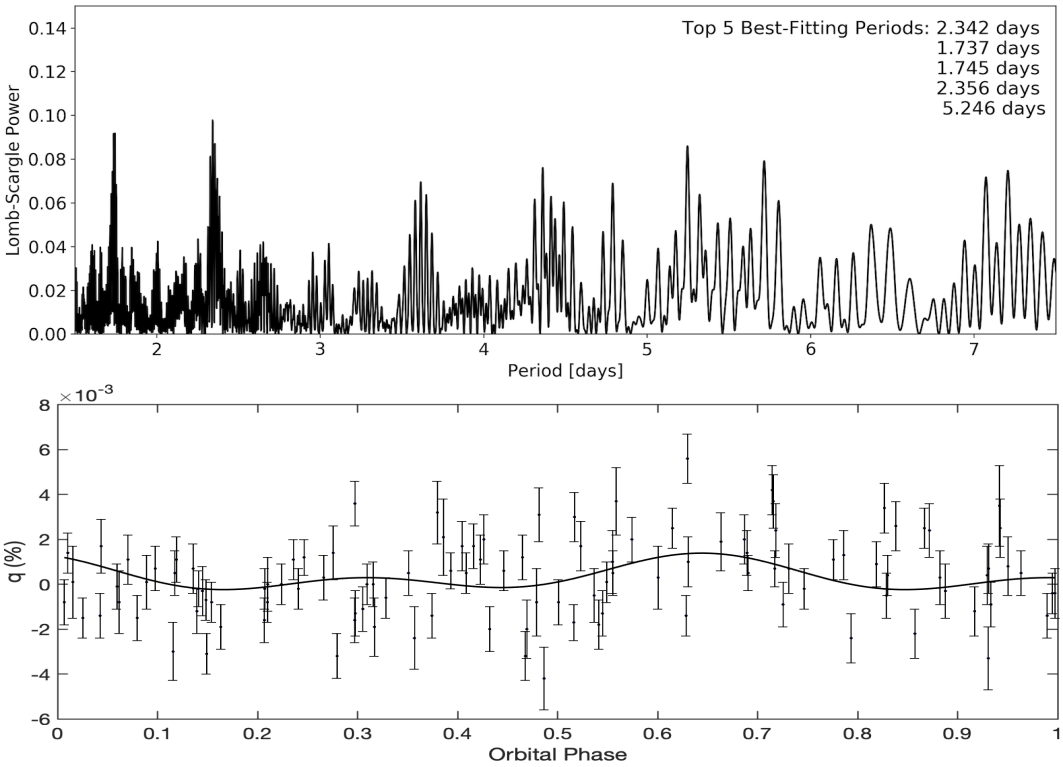

Figure 13. Stokes q in B passband. Lomb-Scargle periodogram in the upper graph and the lower graph is phase folded with orbital period P = 2.342d curve fitting plot.

Lomb-Scargle periodogram of *Stokes q* for *B* passband in Figure 13 shows that there is no single clear peak but instead a few peaks with similar heights. A couple of peaks can be seen at ∼2.3 days and then another couple of peaks at ∼1.7 days. Five highest peaks detected by Lomb Scargle algorithm are also printed out in the top right section of the periodogram. In curve fitting plot of Figure 13, inputs were normalized in order for the curve to better represent variations. Since this data is very noisy due to the presence of multiple orbital periods, any statistical method to verify goodness of the fit would not produce a meaningful result.

To check if similar peaks are present in the data of *Stokes u* for *B* passband, it is also plotted and shown in Figure 14. It can be seen that there are three higher peaks at ∼2.2, ∼1.8 and ∼3.9 days. The periodograms of both *Stokes q* and *u* in *B* passband seem to have repeated a pattern of higher peaks at around the known orbital period of the planet. In the curve fitting plot of Figure 14, *Stokes u* clearly shows variations along the orbital phase.

In Figures 15, the periodogram of *Stokes q* in *V* passband shows that the highest peak is at ∼7.2 days with other higher peaks at ∼1.7 days and ∼2.4 days. Figure 16 shows the periodogram for *Stokes u* in *V* passband. It shows some unique peaks at

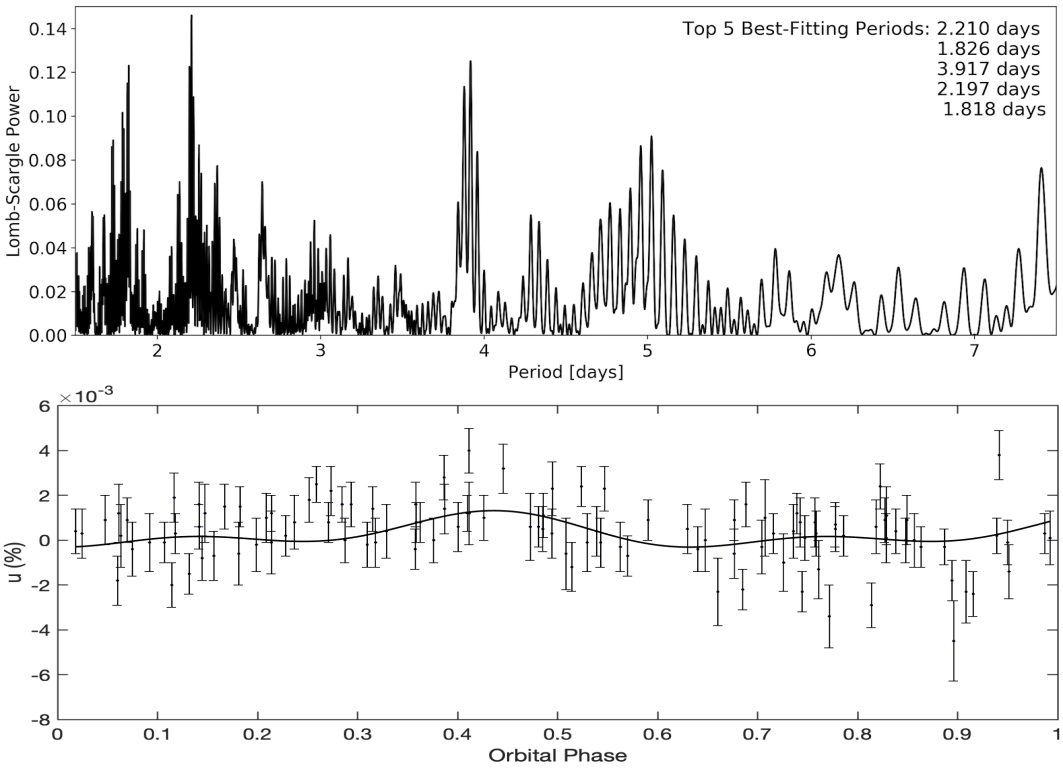

Figure 14. Same as Figure 13 but for Stokes u in B passband and curve fitting plot for P = 2.210d.

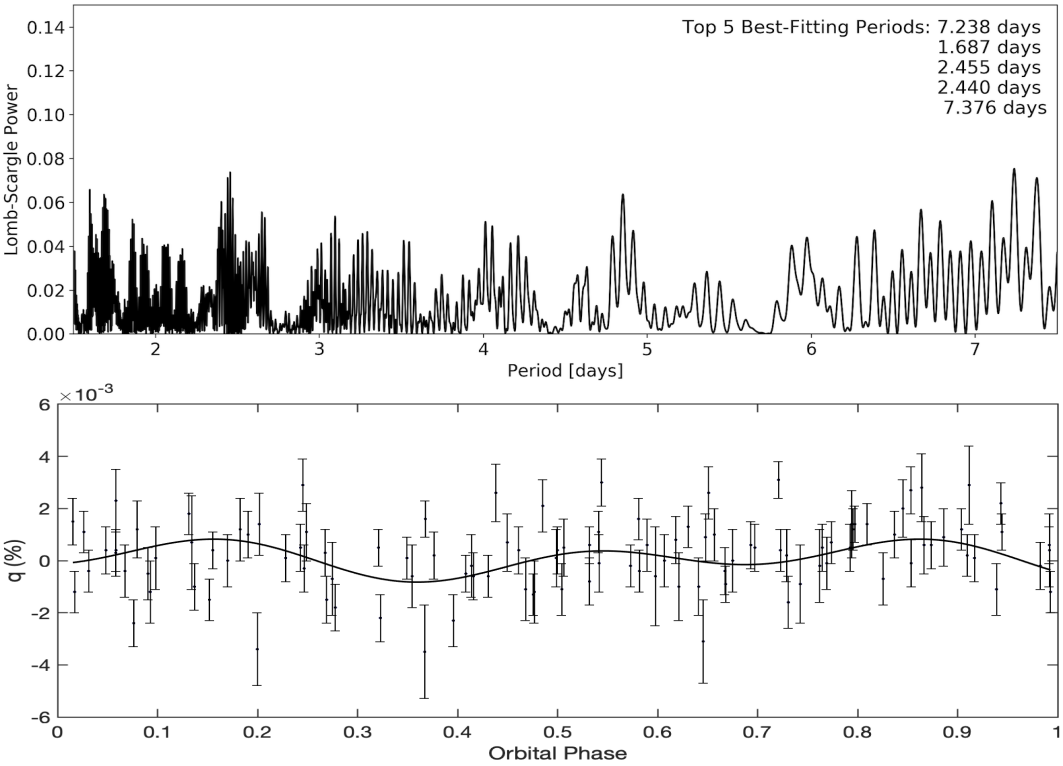

Figure 15. Same as Figure 13 but for Stokes q in V passband and curve fitting plot for P = 2.455d.

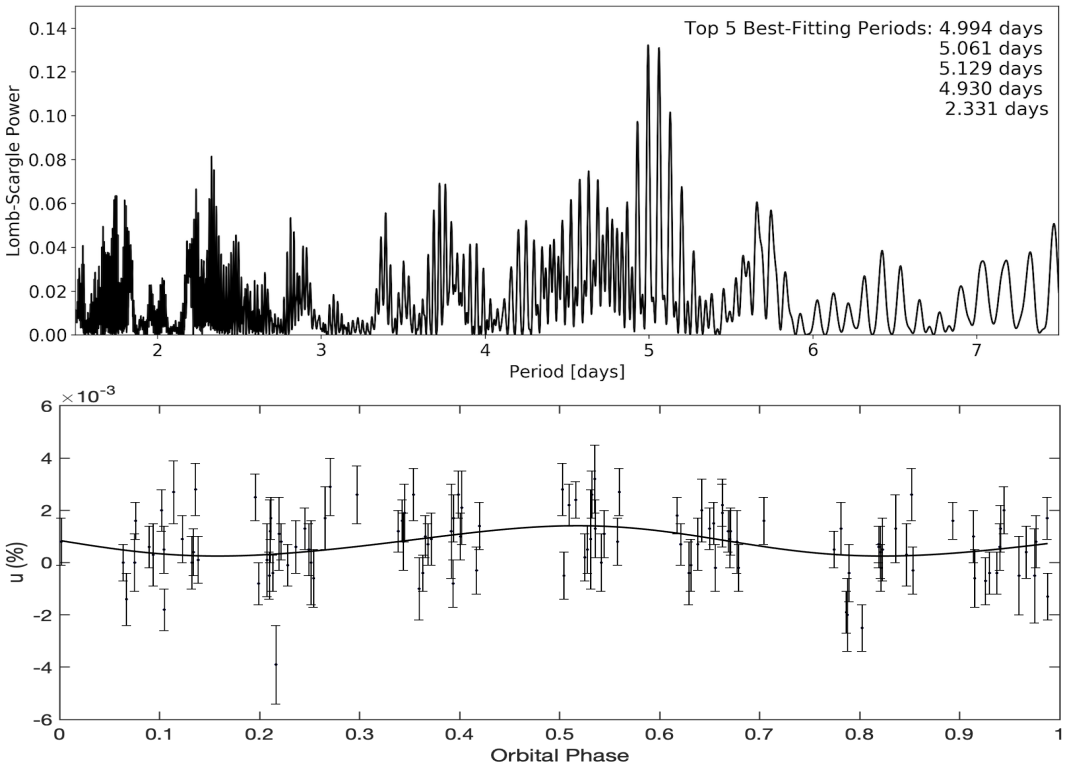

Figure 16. Same as Figure 13 but for Stokes u in V passband and curve fitting plot for P = 2.331d.

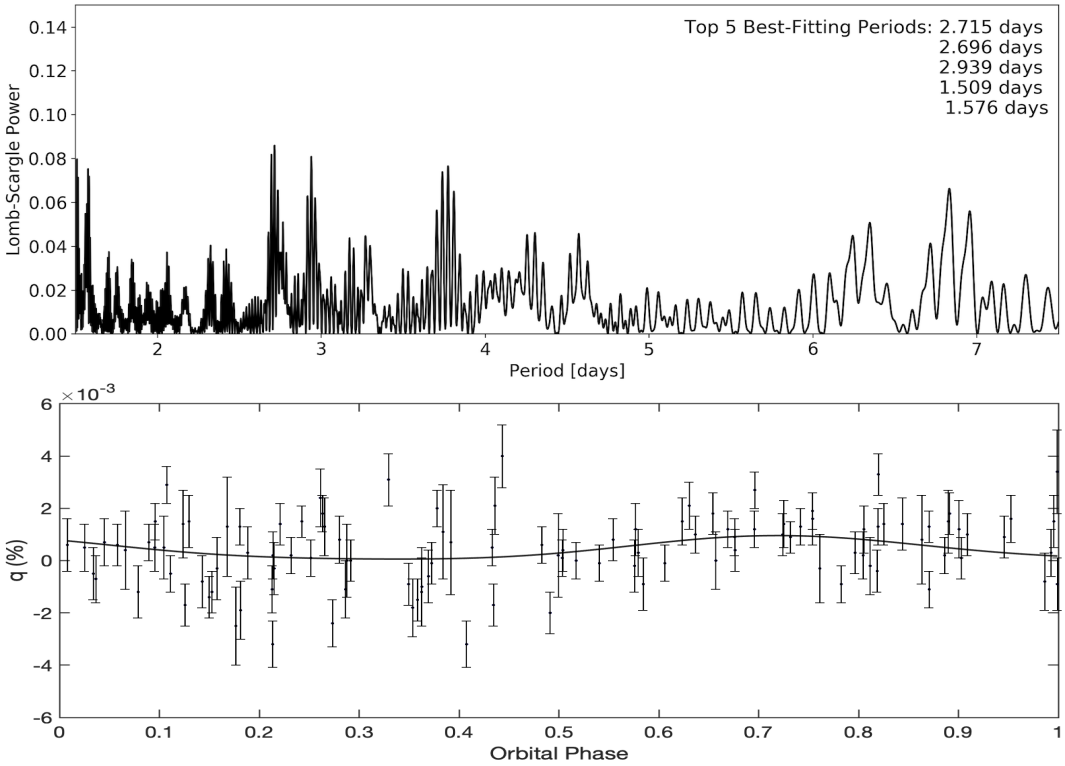

Figure 17. Same as Figure 13 but for Stokes q in R passband and curve fitting plot for P = 2.715d.

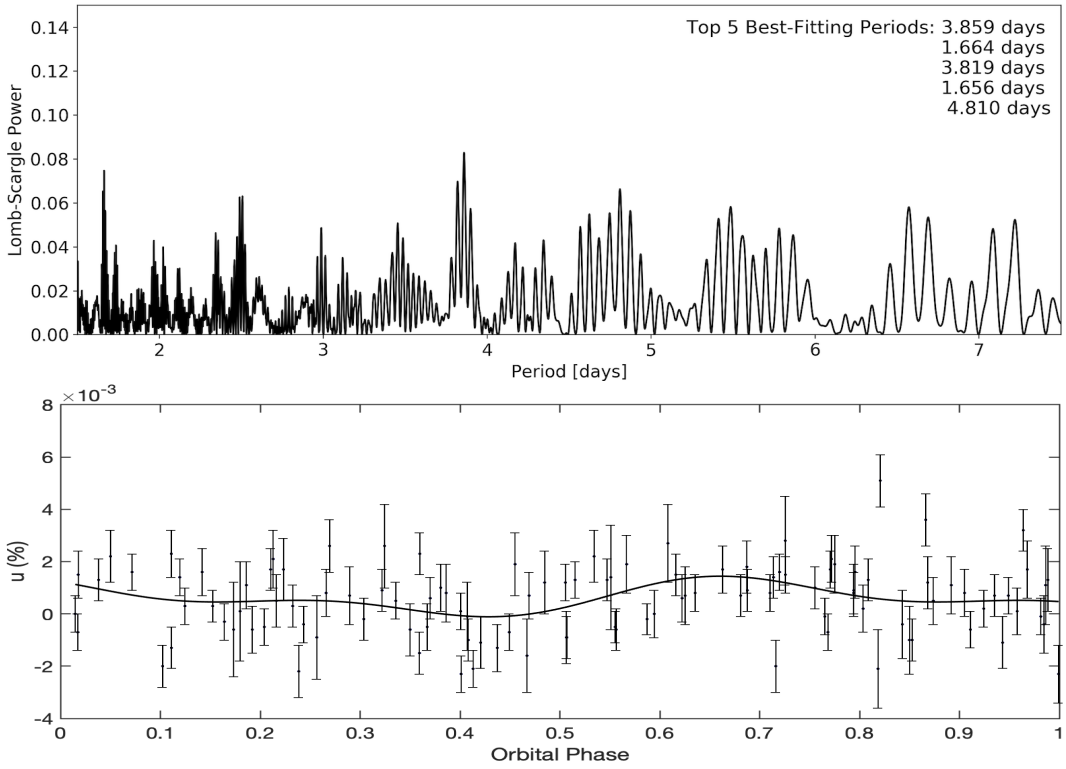

Figure 18. Same as Figure 13 but for Stokes u in R passband and curve fitting plot for P = 2.507d.

∼5 days that are not as clear or higher in other periodograms but they are present in some of them. The other higher peaks are present at ∼2.3 days and ∼1.7 days. The curve fitting plots in Figures 15-16 show clear variations for both *Stokes* q and u.

Figures 17-18 show *Stokes* q and u in R passband respectively. The highest peak for *Stokes* q in R passband is at ∼2.7 days. A couple of other higher peaks are at ∼2.7 days and at ∼1.5 days. The periodogram of *Stokes* u in R passband has the highest peak at ∼3.85 days and a couple of other higher peaks at ∼1.65 days. The peaks are also present at ∼2.5 days but not as clear. The curve fitting plots for both *Stokes* q and u for R passband also show variations along the orbital phase.

4.4 Planetary Characterization of Upsilon Andromedae b

In order to obtain any information for the planetary atmosphere of υ And b, degree of linear polarization (p_L) in terms of normalized Stokes parameters was deduced by using the following equation:

$$p_L = \sqrt{q^2 + u^2}. \tag{36}$$

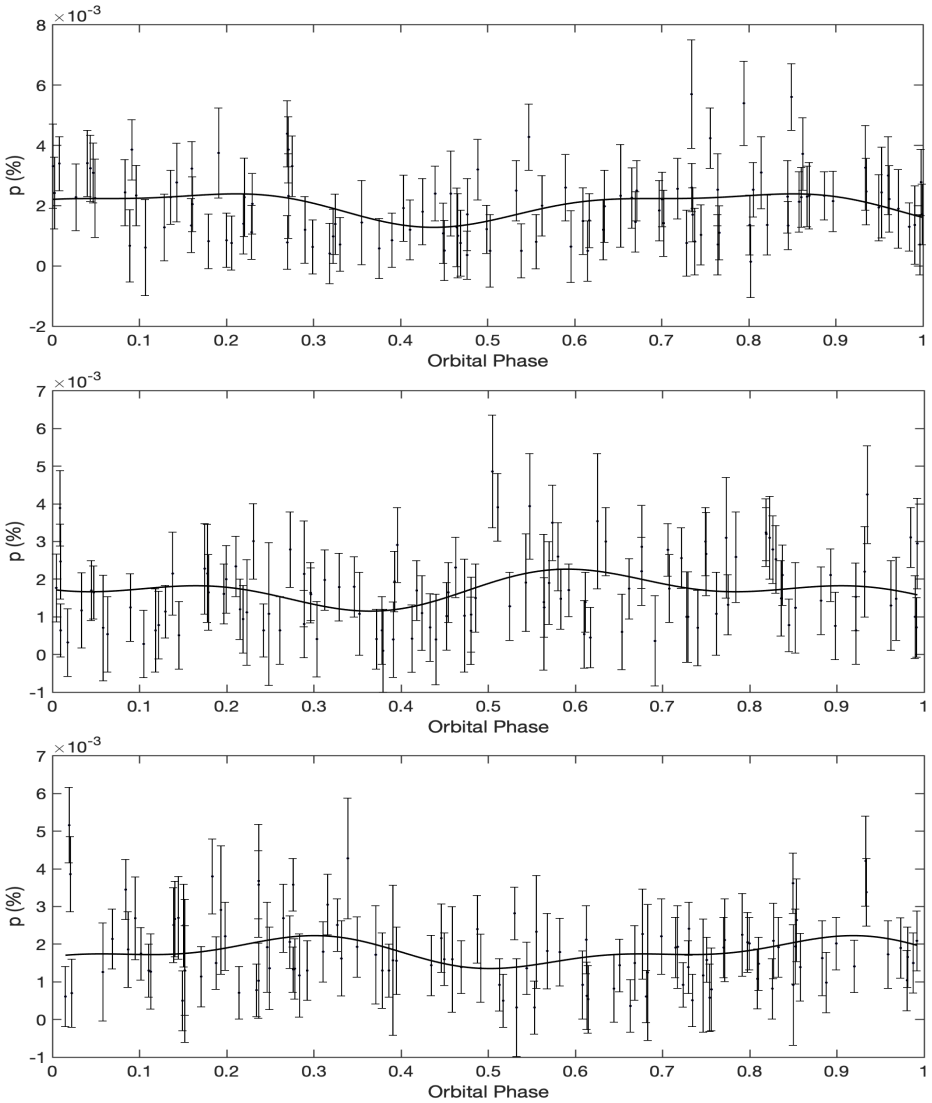

Figure 19. Degree of linear polarization is plotted against phase folded orbital period of υ And b for B, V and R passband in descending order respectively.

The data for all three B, V and R passbands was stored in new files and plotted by slightly modifying the Python script used for the previous section. In order to see the highest peak values, which are needed to estimate geometrical albedo, curve fitting was performed using Equation (34). Figure 19 shows that degree of polarization peaks just above 0.002%, i.e., 2×10^{-5} for all three passbands. Since the data is noisy and peak values are not as accurate, it is not possible to estimate precise geometrical albedo values. However, roughly estimated values are given in Chapter 5.

5 Conclusions

In the last couple of decades with the development of more accurate polarimeters such as DiPol-2, it has now become possible to conduct astronomical polarimetry of numerous objects. By analyzing these polarimetric observations, one can test theories and models that have been written and developed in the past years. The study of exoplanets being one of the most popular topics of astrophysics can now benefit from the use of polarimetry. A number of theoretical models related to the polarimetry of exoplanets are now being tested and new models are being developed.

This study took the advantage of DiPol-2 and T60 to observe a well known star system of Upsilon Andromedae that hosts a CEGP (υ And b). After the lengthy process of observations and data reduction, the analysis of data was performed using a number of mathematical algorithms with the help of Python. The results of data analysis in Chapter 4 when compared to different theoretical models described in Chapter 2, the following conclusions can be drawn:

- There is a possible polarimetric signature of the planetary reflected light and it can be seen in the data of every passbands for both *Stokes* q and u. Lomb-Scargle periodograms repeatedly showed a peak between 2.21 to 2.71 days. As mentioned earlier, the polarimetry of exoplanets shows two peaks during a single orbit and therefore the actual orbital period is twice the values found by Lomb-Scargle peaks, i.e., 4.42 to 5.42 days. This range agrees with the orbital period value of 4.62 days given in a number of papers mentioned in Table 2.

- Another possible polarimetric signature of stellar scattered light due to unevenly distributed starspots on the stellar disk that also vary with time was detected at 1.66 days to 1.82 days. This is an integer sub-multiple of the stellar rotation period of about 7.88 days (Berdyugina et al 2011), which is due to the magnetic activity of the star (possible starspots). A repetition of peaks at 3.7 days to 3.9 days in a number of Lomb-Scargle periodograms correspond to half of the stellar rotational period. Another repetition of peaks at $\sim$5 days is also

observed in several periodograms which may be due to some odd sub-multiple of the stellar rotation period. This conclusion basically confirms a number of points that are mentioned in section 2.3.

- The polarimetric data of υ And b is contaminated by the quarter of stellar rotational period as both values are quite close to each other. In order to precisely fit these entangled polarimetric signals, the development of a more sophisticated model is required. One possible approach can be to map the spot distribution on the surface of υ And, e.g. by Doppler Tomography method and then model their polarization effect. This method, however, would require high-resolution and high signal to noise (S/N) ratio spectroscopic observations.

- The stellar polarization, depending on configuration and location of starspots may have direction nearly orthogonal to the direction of polarization due to exoplanet. This may have resulted in the amplitude reduction of planetary polarization for υ And b. However, polarization peaks given in Figure 19 do not differ much from peaks given by Seager et al (2000) and shown in Figure 6. By using values of these peaks, referring to section 2.2.2 and going through a number of plots given in Seager et al (2000), the roughly estimated value of geometric albedo for υ And b is $p \approx 0.55$. This is deduced by assumjng atmospheric particles with mean radius $\bar{r} = 0.1\mu m$, for which fraction polarization value peaks at $\sim 10^{-5}$ for $i = 90^{\circ}$.

- Equation (35) was used to deduce orbital inclination but values were slightly different for each passband. Even though, the deduced values did not seem quite inaccurate but due to the noisy nature of data, it was decided not to publish them. This is due to the fact that noisy data tends to give a higher value than the actual value.

In order to further refine the findings of this study and extract more information from the observed data, a numerical procedure to separate or clear the orbital periods from a Lomb-Scargle periodogram is required. A newly released R programming language routine named *spectral* has an option to reconstruct a signal from any given Lomb-Scargle peak. It was tried but this routine assumes the signal to be a regular sinusoidal curve and therefore it did not produce the right result. Furthermore, it is possible to do inverse fft (ifft) in order to reconstruct a signal. Non-equispaced fft (nfft) is used for unevenly spaced data and it was tried but it too did not work due to very low amplitude variability and very high uncertainty measurements in this data. Lomb-Scargle algorithm as expected turns out to be more powerful than fft methods

for uneven sampling and it was the only tried algorithm to plot a periodogram that showed right orbital periods of υ And data. In future, a model that can separate asymmetric periods given by a Lomb-Scargle periodogram should be able to further advance this research work.

References

[1] A.V. Berdyugin, V. Piirola and J. Poutanen, Astrophysics and Space Science Library **460** (2019) pp. 33-65.

[2] S. Trippe, Journal of The Korean Astronomical Society **47**, 15 (2014).

[3] G.B. Rybicki and A.P. Lightman, Radiative Processes in Astrophysics (Wiley and Sons 1979) pp. 62-29.

[4] V. Piirola, A.V. Berdyugin and Svetlana Berdyugina, "DiPol-2: a double image high precision polarimeter," Proc. SPIE 9147, Ground-based and Airborne Instrumentation for Astronomy V, 91478I (28 July 2014).

[5] M. Planck, Annalen der Physik, **4**, 553 (1901).

[6] S. Bagnulo and J.D. Landstreet, Polarimetry of Stars and Planetary Systems, Edited by L. Kolokolova, J. Hough, and A. Levasseur-Regourd. (Cambridge University Press 2015) pp. 224-243.

[7] G.A. Wade *et al.*, Astronomy & Astrophysics **374**, 265–279 (2001).

[8] T.M. Yakobchuk and S.V. Berdyugina, Astronomy & Astrophysics **613**, A7 (2018).

[9] S.V. Berdyugina, Living Reviews in Solar Physics, **2**, 8 (2005).

[10] B. H. Zellner and K. Serkowski, Publications of the Astronomical Society of the Pacific Vol. 84, No. 501 (October 1972), pp. 619-626.

[11] E. Bowell and B. Zellner, Planets, Stars, and Nebulae: Studied with Photopolarimetry, Proceedinsg of IAU Colloq. 23, held in Tucson, AZ, November, 1972. Edited by T. Gehrels. (University of Arizona Press 1974) pp. 382-384.

[12] S. Seager, B.A. Whitney and D.D. Sasselov, The Astrophysical Journal **540**, 504-520 (2000).

[13] M. Starr, "That Interstellar Comet Is Carrying Water From Beyond Our Solar System". ScienceAlert.com (Retrieved 02 March 2020).

[14] S.V. Berdyugina *et al.*, The Astrophysical Journal **673**, L83–L86, (2008).

[15] D.M. Fluri and S.V. Berdyugina, Astronomy & Astrophysics **512**, A59 (2010).

[16] S.V. Berdyugina, A.V. Berdyugin and V. Piirola, arXiv:1109.3116v1 [astro-ph.EP] (2011).

[17] H.N. Russell, The Astrophysical Journal, **43**, 173 (1916).

[18] S.J. Wiktorowicz and D.M. Stam, Polarimetry of Stars and Planetary Systems, Edited by L. Kolokolova, J. Hough, and A. Levasseur-Regourd. (Cambridge University Press 2015) pp.439-461.

[19] D. Sudarsky *et al.*, The Astrophysical Journal, **627**, 520 (2005).

[20] A.C. Cameron *et al.*, Nature, **402**, 751 (1999).

[21] D. Charbonneau *et al.*, The Astrophysical Journal, **522**, L145 (1999). .

[22] J.E. Hansen, J.W. Hovenier, Journal of Atmospheric Science, **31**, 1137 - 1160 (1974).

[23] L. Kedziora-Chudczer, J. Bailey, Pathways Towards Habitable Planets, proceedings of a workshop held 14 to 18 September 2009 in Barcelona, Spain. Edited by Vincent Coudé du Foresto, Dawn M. Gelino, and Ignasi Ribas. San Francisco: Astronomical Society of the Pacific (October 2010) p.469.

[24] N.M. Kostogryz, T.M. Yakobchuk and S.V. Berdyugina, The Astrophysical Journal **806**, 97 (2015).

[25] N.M. Kostogryz *et al.*, Astronomy & Astrophysics **586**, A87 (2016).

[26] D. Clarke, Astronomy & Astrophysics **407**, 1029–1037 (2003).

[27] R.P. Butler *et al.*, The Astrophysical Journal **646**, 505 (2006).

[28] B.E. McArthur *et al.*, The Astrophysical Journal **715**, 1203 (2010).

[29] S. Curiel *et al.*, Astronomy & Astrophysics, **525**, A78 (2011).

[30] V. Piirola, A.V. Berdyugin, and S.V. Berdyugina, "DiPol-2: a double image high precision polarimeter", Proc. SPIE 9147, Ground-based and Airborne Instrumentation for Astronomy V, 91478I (28 July 2014).

[31] J.C. Brown, I.S. McLean and A.G. Emslie, Astronomy & Astrophysics, **68**, 415 (1978).

[32] R.J. Rudy and J.C. Kemp, The Astrophysical Journal **221**, 200 (1978).

[33] M.E. Zugger *et al.*, The Astrophysical Journal, **723**, Issue 2, (2010) pp. 1168-1179.

[34] N. Madhusudhan and A. Burrows, The Astrophysical Journal, **747/1**, 25 (2012).

[35] S.J. Wiktorowicz1 and G.P. Laughlin, The Astrophysical Journal, **795**, 12 (2014).

[36] S.Sengupta The Astrophysical Journal, **152**, 4 (2016).

[37] J.T. VanderPlas, The Astrophysical Journal Supplement Series, **236/1**, 16 (2018).

[38] L.M. Serrano *et al.*, Astronomy & Astrophysics, **611**, A8 (2018).

[39] N.R. Lomb, Astrophysics & Space Science **39**, 447 (1976).

[40] C. Heiles, ASP Conference Proceedings, Vol. 278. San Francisco: Astronomical Society of the Pacific (2002) pp. 131-152.

[41] S. Saar, S. Seager, ASP Conference Series, **294**, 529 (2003).

[42] D. M. Stam, J.W. Hovenier and L.B.F.M. Waters Astronomy & Astrophysics **428**, 663–672 (2004).

[43] S.V. Berdyugina *et al.*, The Astrophysical Journal, **673**, L83–L86 (2008).

[44] J. Tinbergen, Astronomical Polarimetry (Cambridge University Press September 1996) pp. 174.

[45] J.D. Hartman, The Astrophysical Journal, **728/2**, 138 (2011).

[46] D.M. Stam *et al.*, Astronomy & Astrophysics, **452**, 669–683 (2006).

[47] S.V. Berdyugina, arXiv:1607.06874v1 [astro-ph.EP] (2016).

[48] N. Manset, P. Bastien, The Astronomical Journal **122**, 6 (2001).

[49] D.M. Stam, Proceedings of the Conference on Towards Other Earths: DARWIN/TPF and the Search for Extrasolar Terrestrial Planets (Noordwijk: ESA 2003) pp. 615-619.

[50] T. Shahbaz, Astrophysics and Space Science Library, **460**, 247-276 (2019).

[51] V. Piirola, The Astrophysical Journal, **632/1**, 576-589 (2005).

[52] J. Duoandikoetxea, Fourier analysis: Graduate Studies in Mathematics, (AMS, Providence Rhode Island, 2001).

[53] F. Martins, L. Mahy and A. Hervé, Astronomy & Astrophysics, **607**, A82 (2017).

[54] P. Goldreich and N.D. Kylafis, The Astrophysical Journal, **253**, 606 (1982)

[55] M. Zechmeister and M. Kürster Astronomy & Astrophysics, **496**, 577–584 (2009).